J. Fluid Mech. (2005), *vol.* 522, *pp.* 141–177.
DOI: 10.1017/S0022112004001727 Printed in the United Kingdom

Velocity fields in mixing-enhanced compressible shear layers

By SHIGEYA WATANABE[1] AND M. G. MUNGAL[2]

[1]Wind Tunnel Technology Center, Japan Aerospace Exploration Agency, Chofu, Tokyo 182-8522, Japan

[2]Mechanical Engineering Department, Stanford University, Stanford, CA 94305, USA

(Received 24 April 2003 and in revised form 22 July 2004)

Planar velocity fields of mixing-enhanced compressible planar shear layers are measured via particle image velocimetry (PIV) in order to investigate the mechanism of mixing enhancement by sub-boundary-layer triangular disturbances. The measurements are conducted at convective Mach numbers, M_c, of 0.62 and 0.24 to examine compressibility effects on effectiveness of the mixing enhancement technique. Instantaneous side- and plan-view vector maps of the shear layers are obtained, and turbulence statistical quantities are derived from the instantaneous velocity data. Schlieren and planar laser Mie scattering (PLMS) techniques are also used to measure the shear-layer thickness and growth rate as well as surveying the qualitative flow fields. The velocity fields for several disturbance configurations with different shape, size, or thickness are compared in terms of the shear-layer thickness and growth rate in order to investigate the effects of the configuration variation on the mixing enhancement strategy. Configuration parameters include thickness, the semi-vertex angle of the triangular disturbance, and the streamwise offset of the disturbance from the splitter tip. The measured transverse profile of the mean streamwise velocity shows a characteristic shape with triple inflection points for the effective mixing-enhanced cases at the two different compressibility conditions, while periodic inflection points are observed in the spanwise direction. A pair of stationary counter-rotating streamwise vortices introduced by the subboundary-layer disturbances are also observed, even in the fully developed region of the shear layers. At $M_c = 0.62$, it is found that in successfully enhanced cases, regardless of the disturbance configurations, the present mixing-enhancement strategy has the effect of increasing the turbulence intensity and Reynolds stress, and suppressing the turbulence anisotropy increase with increasing compressibility, i.e. alleviating the compressibility effect which intrinsically reduces pressure–strain-rate redistribution, leading to effective mixing enhancement. Comparison of the results at the two compressibility conditions reveals that the growth rate of the layer is almost constant in the streamwise direction for all cases at $M_c = 0.62$, while for all disturbed cases at $M_c = 0.24$, after an initial layer thickening, growth rate decreases with downstream distance to the value for the undisturbed case, indicating that the present mixing enhancement is less effective at nearly incompressible conditions.

1. Introduction

1.1. *Background and motivation*

With renewed interest in supersonic combustion ramjets (scramjets) and noise reduction for the high-speed civil transport, experimental and numerical studies on compressible shear layers have been conducted extensively for the past two decades with

the purpose of developing techniques to control such flows based on the proper understanding of the flow phenomena.

Focusing on the scramjet, one of the main technological challenges is the effective mixing of air and fuel in the combustor at compressible (supersonic) conditions. The combination of two issues makes the problem difficult to solve: (i) supersonic flow in the combustor of restricted length means very short residence time (e.g. order of tens of microseconds) for mixing and combustion (see, for example, Ferri 1973; Swithenbank *et al.* 1991), and (ii) compressibility causes poor mixing relative to incompressible cases because of a reduced growth rate of the shear layers in the combustor. In order to solve the problem, techniques to keep mixing efficiency high with a minimum total pressure loss are required. One of the solutions for meeting the requirements simultaneously could be to adopt a parallel fuel injection strategy with effective mixing-enhancement techniques. The most fundamental flow model simulating mixing in the scramjet combustor with parallel fuel injection is the 'planar compressible shear layer'. Thus, it is of significance for development of effective mixing enhancements to quantitatively measure mixing-enhanced compressible shear layers in detail by means of advanced velocity measurement techniques, such as particle image velocimetry (PIV) (e.g. Adrian 1991).

1.2. *Planar compressible shear layer*

Extensive investigations of compressible shear layers have been conducted experimentally, analytically and numerically in the last two decades, originating from a question on growth rate difference at different compressibility conditions. One of the most important advances in compressible studies was to extract a global parameter characterizing the effect of compressibility, namely the *convective Mach number*, M_c (Bogdanoff 1983; Papamoschou & Roshko 1988), which is defined (for the case with identical specific heat ratios for high- and low-speed streams, $\gamma_1 = \gamma_2$) by

$$M_c = M_{c_1} = M_{c_2} = \frac{U_1 - U_2}{a_1 + a_2}, \tag{1.1}$$

where M_{c_1}, M_{c_2}, U_1, U_2 and a_1, a_2 are convective Mach numbers, free-stream velocities, and speeds of sound for the high-speed and low-speed streams, respectively. The corresponding *convective velocity*, U_c, at which the structure embedded in the shear layer convects is defined by

$$U_c = \frac{a_2 U_1 + a_1 U_2}{a_1 + a_2}. \tag{1.2}$$

Experimental data (e.g. Chinzei *et al.* 1986; Papamoschou & Roshko 1988; Elliott & Samimy 1990; Goebel & Dutton 1991; Clemens & Mungal 1992*b*) have shown that the convective Mach number is a generally suitable correlation parameter for the compressibility effect. Also, the results revealed a clear trend of reduced growth rate with increasing M_c. Linear stability growth rate analyses exhibited similar reduction with increase in M_c (e.g. Ragab & Wu 1989; Sandham & Reynolds 1990).

Evidence of shear-layer structure transition with increasing compressibility has been obtained mainly by experimental studies. Using flow visualization via planar laser Mie scattering (PLMS) and planar laser-induced fluorescence (PLIF) techniques, Clemens & Mungal (1992*b*, 1995) concluded that with increasing compressibility, the eddy structure embedded in the shear layer changes from quasi-two-dimensional large-scale structures at incompressible conditions to three-dimensional oblique structures at $M_c > 0.6$. Combining linear stability analysis and direct numerical simulations,

Sandham & Reynolds (1990, 1991) presented results consistent with the corresponding experimental data.

Extensive measurements via laser-Doppler velocimetry (LDV) and particle image velocimetry (PIV) have added useful information on turbulence statistics and velocity fields. Elliott & Samimy (1990) and Goebel & Dutton (1991) gave us detailed pointwise velocity measurement results from two-component LDV in a M_c range from 0.20 to 0.99. Both studies found that transverse turbulence intensity σ_v and Reynolds stress $\langle u'v' \rangle$ significantly reduces as compressibility increases. On the other hand, Goebel & Dutton's (1991) results did not show a distinct change of streamwise turbulence intensity σ_u, leading to an increase in anisotropy σ_u/σ_v with increasing compressibility, while decrease in σ_u with increasing M_c was observed by Elliott & Samimy (1990). A three-component LDV study by Gruber, Messersmith & Dutton (1993) supported the conclusion for the anisotropy by Goebel & Dutton (1991) and found a trend of nearly constant $\sigma_w$with increasing M_c. However, a direct numerical simulation for a turbulent annular mixing layer covering a wide M_c range from 0.1 to 1.8 (Freund, Lele & Moin 2000) found a decreasing azimuthal turbulence intensity, which corresponds to σ_w for the planar shear layer, with increased compressibility.

Benefiting from the recent technological progress of PIV, Urban & Mungal (1997) conducted initial two-dimensional instantaneous velocity field measurements of a planar shear layer at $M_c = 0.63$. Afterwards, additional extensive measurements were conducted at $M_c = 0.25$ and 0.76 (Urban, Watanabe & Mungal 1998; Urban 1999; Urban & Mungal 2001) to investigate compressibility effects. Taking advantage of the instantaneous planar measurement ability of PIV, the results showed that compressibility causes changes to the disposition of instantaneous velocity gradients within the layer, and transverse vorticity is confined to thin streamwise sheets with little transverse communication, leading to growth rate suppression. Other PIV measurements were made by Olsen & Dutton (2003) for a weakly compressible mixing layer ($M_c = 0.38$). They calculated spatial correlations of velocity fluctuations, finding that the correlations are a smaller fraction of the mixing-layer thickness than the incompressible counterpart.

For more comprehensive surveys, see, for example, Dimotakis (1991), Lele (1994) and Dutton (1997).

1.3. *Mixing enhancement of the compressible shear layer*

As reviewed by Gutmark, Schadow & Yu (1995), numerous techniques have been tried to enhance mixing in different types of compressible shear flows. Here, passive mixing-enhancement techniques mainly for planar compressible shear layers are briefly introduced.

Ideas for the mixing enhancements of the compressible shear layer can be generally categorized into several types including: (i) shock wave impingement onto the shear layer, (ii) excitation of shear layer instabilities, and (iii) introduction of streamwise vorticity. The first category consists of two-dimensional and three-dimensional approaches. Menon (1989) used a two-dimensional shock generated by a wedge mounted on the supersonic-side ($M = 2.5$) wall, resulting in a significantly thickened shear layer downstream of the shock/shear layer interaction region. Samimy, Erwin & Elliott (1989) put an obstacle in the shear layer at M_c of 0.51 and 0.86 to generate a two-dimensional bow shock in the high-speed stream. The results showed a slight increase in growth rate with a large total pressure loss. On the other hand, Clemens & Mungal (1992*a*) impinged a shock perpendicular to the shear-layer plane in a three-dimensional fashion by mounting a line bump on the sidewall at $M_c = 0.3$ and 0.6.

They found a significant deformation of the shear layer in its cross-sectional shape without apparent change in thickness, meaning an increased amount of mixed fluid in the elongated shear layer.

The second type of mixing enhancement can be accomplished by mounting a cavity on the high-speed sidewall to generate acoustic waves impinging on the shear layer (Sato *et al.* 1999). The results at $M_c = 0.62$ indicated that the shear layer oscillates with increased instability, leading to an increase in growth rate, at least in the near field.

The majority in the third category employ modification of the splitter tip. Trailing-edge devices with circular cylinders and corrugated plate arrangements were investigated by Dolling, Fournier & Shau (1992), leading to thicker shear layers owing to thickened boundary layers on the splitter plate while the growth rate stayed almost unchanged. Fernando & Menon (1993) found apparent increases in near-field growth rate as well as local thickening for several three-dimensional trailing-edge devices with a tooth geometry at M_c less than 0.5.

From the present overview, it can be concluded that the global shear-layer growth rate in the far field or self-similar region has hardly been increased or not measured because of experimental restrictions, whereas some techniques succeeded in locally thickening the shear layer and enhancing near-field growth rate. Also, it should be noted that even if growth rate improvements can be attained by introducing large disturbances, severe total pressure losses due to the disturbances could outweigh the benefits of the enhanced mixing.

Contrary to the unsuccessful mixing enhancements of the planar compressible shear layer, Island, Urban & Mungal (1998) observed a significant (i.e. about 50%) increase in the global growth rate at a moderate compressibility condition, $M_c = 0.63$, by employing triangular-shaped disturbances of sub-boundary-layer thickness located at the high-speed side splitter tip. It is significant that their mixing enhancement is obtained with a minimal total pressure loss owing to weak shocks generated from the device, and that the enhanced growth rate sustains itself into the fully developed region, indicating a global effect rather than an initial one. In their study, mixing-enhancement effects of several disturbance configurations with different size, shape and location were investigated qualitatively and quantitatively by using PLMS, PLIF and schlieren techniques. Based on the results, an optimum configuration was chosen from those tested. Also, it was revealed that the disturbance induces appreciable spanwise convolution and streamwise structure, and causes a slight mixing efficiency increase up to 7% and a large increase in the layer thickness by 48%, indicating that gains in the total amount of mixed fluid occur primarily by layer thickening.

1.4. *Objectives*

Although Island *et al.* (1998) conducted extensive scalar measurements, it seems that the scalar information is not enough to understand fully what is happening in the enhanced layer. Also, the measurement was conducted at only one moderate compressibility condition, thereby lacking information on the effectiveness of the mixing-enhancement strategy with compressibility.

In the present study, employing Island *et al.*'s (1998) mixing-enhancement technique, instantaneous velocity fields in the mixing-enhanced compressible shear layers are measured via two-dimensional PIV in order to investigate the mechanism of the mixing enhancement which has not been sufficiently understood by the scalar measurements alone. Based on the instantaneous vector maps, turbulence statistical properties are derived. Compressibility effects on the mixing enhancement are also investigated by

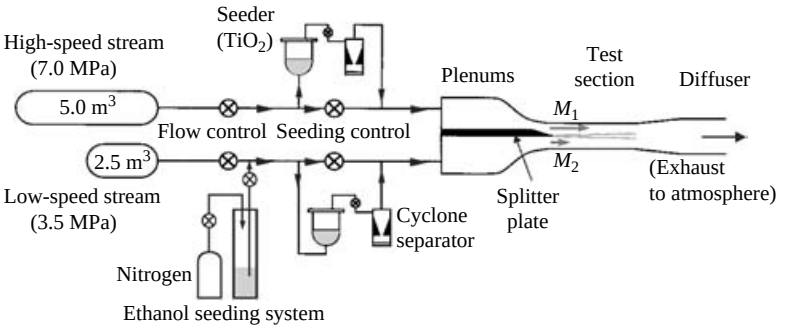

FIGURE 1. Supersonic mixing and combustion wind tunnel.

comparing results measured at two different compressibility conditions, i.e. $M_c = 0.62$ (moderate compressibility) and 0.24 (a nearly incompressible condition). The schlieren technique is also used to survey the mixing-enhanced shear layer covering a large streamwise distance. Flow fields with various disturbance configurations are also measured to correlate the effectiveness of the technique (i.e. growth rate or thickness) with quantities identified in the velocity fields. The PLMS technique is used to measure the shear-layer thickness and growth rate considering spanwise distribution as well as to acquire time- and spatially-resolved images of the flow structure in the shear layer. In this study, it is assumed that the growth rate or shear-layer thickness is nearly proportional to the amount of the molecularly mixed fluid, since the previous PLIF results (Island *et al.* 1998) showed only a small increase of mixing efficiency due to the present disturbances for enhancing mixing.

In the remainder of this paper, the experimental facility and measurement techniques are introduced in § 2 as well as the test conditions. The measurement results for the optimum disturbance configuration are presented and discussed in § 3. Then, the results for the various disturbance configurations are compared in § 4, followed by conclusions (§ 5) derived from the present experimental investigation.

2. Experimental method

2.1. *Wind-tunnel and test conditions*

The flow facility used in this study is a blow-down-type supersonic wind tunnel specially designed for mixing and combustion research on compressible planar shear layers. The schematic of the facility is shown in figure 1. This wind tunnel has two high-pressure tanks to generate a planar shear layer between two free streams with different speeds at the test section. In the present test, the high-speed stream was supersonic while the low-speed flow was subsonic for all runs. The static pressure of the two streams is individually regulated to ensure pressure matching at the nozzle exits, that is, the splitter tip (0.7 mm thick). The size of the flow path in the test section is $45 \times 8 \times 10\,\mathrm{cm}^3$ in streamwise (x), transverse (y), and spanwise (z) directions, respectively, while the height changes slightly in the streamwise direction. Seven wall pressure taps are located on the upper and lower walls of the test section to measure the streamwise variation of the static pressure. Fused silica windows on the upper, lower and sidewalls provide optical access for side- and plan-views of PIV as well as the schlieren and PLMS. The compressibility of the mixing layer represented by M_c is varied by changing the nozzle exit Mach numbers (i.e. nozzle shapes) in this study.

Case	$M_c = 0.24$		$M_c = 0.62$	
Stream	1	2	1	2
Bulk gas	Air	Air	Air	Air
M_{ex}	1.49	0.82	2.18	0.50
δ_{99} (mm)	1.6	1.0–1.5	1.6	1.0–1.5
θ (mm)	0.15	–	0.12	–
M_{img}	1.60	0.96	2.14	0.51
T_{img} (K)	179	228	141	257
U_{img} (m s^{-1})	428	291	509	162
U_c (m s^{-1})	364		362	
$r \equiv U_2/U_1$	0.68		0.32	
$s \equiv \rho_2/\rho_1$	0.78		0.50	
δ_{nd} (mm)	14.5		13.4	
$Re_{\delta_{nd}}$	1.7×10^5		4.4×10^5	
x_{img} (mm)	360		220	
x_{img}/θ	2400		1830	
Rx_{img}/λ	16		31	

TABLE 1. Test conditions: M_{ex} is the nozzle exit Mach number, δ_{99} the 99%-velocity thickness of the high-speed side boundary layer at the splitter tip, θ momentum thickness corresponding to δ_{99} (calculated by Clemens 1991), $Re_{\delta_{nd}}$ Reynolds number based on shear-layer thickness between 5 and 95% velocity points at imaging station for no-disturbance case, R velocity ratio ($=(1-r)/(1+r)$), λ initial stability wavelength ($\approx 30\theta$), and subscript '*img*' denotes values measured at the PIV imaging station.

Details of this facility are extensively described by Clemens (1991), Miller (1994), Island (1997) and Urban (1999).

Titanium dioxide (TiO_2) particles are introduced as seed for the PIV measurement into both streams upstream of the plenum chambers through pressurized fluidized beds and cyclone separators (Urban 1999). For the PLMS measurements, liquid ethanol is sprayed into only the low-speed stream well upstream of the plenum chamber against the flow, which fully evaporates before reaching the test section.

Table 1 shows the test conditions including characteristic parameters about the boundary layer on the splitter plate. The experiments were conducted mainly at a moderate convective Mach number M_c of 0.62 while data were also acquired at $M_c = 0.24$ to investigate the compressibility effect. The supply gas for both streams was air at ambient temperature at the stagnation condition. Former schlieren observations (Clemens 1991) confirmed that the boundary layer on the high-speed side of the splitter plate is turbulent as expected from the Reynolds number based on the momentum thickness calculated by a turbulent boundary-layer code, and that the calculated boundary-layer thickness in table 1 is reasonable. The Reynolds number based on the shear-layer thickness at the imaging locations for the no-disturbance case are 1.7×10^5 and 4.4×10^5 at $M_c = 0.24$ and 0.62, respectively. According to the modified Bradshaw's criterion (Goebel & Dutton 1991), the shear layers at the imaging stations are expected to be in nearly fully developed conditions (Clemens 1991). Since the 'pairing parameter', Rx_{img}/λ, where $R(\equiv(1-r)/(1+r))$, x_{img}, and λ denote velocity ratio, streamwise imaging location, and initial instability wavelength, respectively, is 16 and 31 at $M_c = 0.24$ and 0.62, respectively, the criterion for the fully developed state for the incompressible case, that is, $Rx/\lambda > 16$ (Karasso & Mungal 1996), confirms this conclusion.

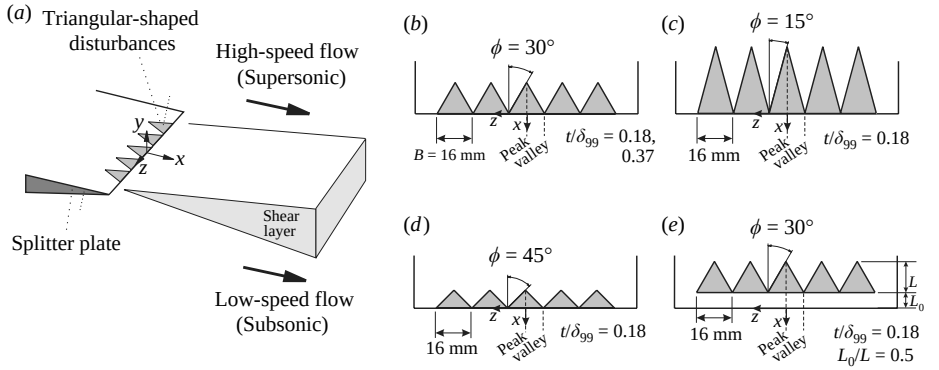

FIGURE 2. Disturbances for mixing enhancement: (*a*) schematic with coordinate definition, and plan-view schematics of (*b*) Case 3, (*c*) Case 4, (*d*) Case 5 and (*e*) Case 6 configurations.

2.2. *Devices for mixing enhancement*

Following the mixing-enhancing technique devised by Island *et al.* (1998), triangular disturbances with sub-boundary-layer thickness were placed on the splitter tip on the high-speed side only, as shown in figure 2. The figure also contains the definition of the coordinates used hereinafter. The thickness of the disturbances was chosen to be much less than the boundary-layer thickness at the tip of the high-speed side splitter plate, δ_{99}, in order to minimize the total pressure loss in the free stream owing to shock waves generated at the leading edges of the disturbances. Acetate tape (commercially referred to as 'Scotch tape') of about 60 μm in thickness was layered to form the disturbances with the specified thickness. The top layer of each disturbance was marked using a red marker in order to check the integrity of the disturbance easily after each wind-tunnel run.

Various triangular disturbances with different configurations were investigated to compare velocity fields in successfully enhanced cases with those in poorly enhanced cases. The width of each disturbance B is set to 1.6 cm for all cases since it was found by Island *et al.* (1998) that this size is nearly optimum at the moderate compressibility level ($M_c = 0.62$). Five identical disturbances are placed at the same streamwise location with no space between them.

Variable parameters of the disturbance configuration in the present experiment consist of (i) thickness t, (ii) semi-vertex angle of a triangular disturbance ϕ, and (iii) offset of the trailing edge of the disturbances from the splitter tip L_0, which is represented below by a parameter (L_0/L) non-dimensionalized by the disturbance streamwise length L (=1.39 cm). To examine the effects of the parameters, four cases of different planform shape or location with identical thickness (Cases 3, 4, 5 and 6) and a case with thicker disturbance with the planform shape of Case 3 were tested while Case 0 was measured as a reference case with no disturbances. The case number follows the numbering rule of the configurations in Island *et al.* (1998). Referencing to the growth rate measurement results by PLMS (Island *et al.* 1998), Case 3, which has the most effective planform shape of an equilateral triangle, is used as the optimum shape among the configurations tested. In Case 3, t was chosen to be both 18% and 37% of the boundary-layer thickness δ_{99} to investigate the effect of the disturbance thickness. It was set to $0.18\,\delta_{99}$ for all the other cases. Cases 3, 4 and 5 form a set of cases to investigate the effects of the semi-vertex angle ϕ. The effect of the streamwise offset of the disturbances can be focused by comparing Case 6 ($L_0/L = 0.5$) with

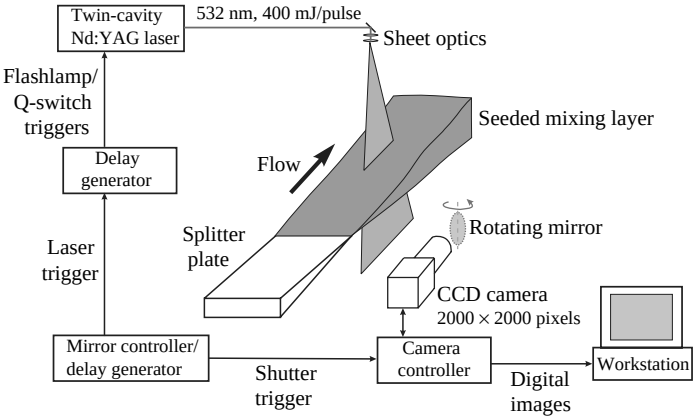

FIGURE 3. PIV system schematic (side-view configuration).

Case 3 ($L_0/L = 0$). For the side-view of PIV or PLMS with a laser light sheet parallel to the (x, y)-plane, two-dimensional velocity or scalar fields on the planes including the disturbance 'peak' and 'valley' (see figure 2) of the centre disturbance element were measured individually to investigate variation of the flow fields in the spanwise direction. For the disturbed cases, the plan-view images with a laser light sheet parallel to the (x, z)-plane were acquired at upper and lower transverse locations, which were chosen so that the streamwise vortices generated by the disturbances could be located between the two transverse locations. For the no-disturbance case, the plan-view images were obtained at only one transverse location in the middle of the shear layer.

2.3. *Planar velocity measurement via PIV*

The two-dimensional PIV system set-up for side-views is shown schematically in figure 3. A two-cavity pulsed Nd:YAG laser (Quanta-Ray PIV-400) is used for illuminating TiO_2 seed particles in the flow. It delivers collinear beams of 532 nm wavelength light at up to 400 mJ per 8 ns laser pulse. A short pulse separation of typically 300 ns for $M_c = 0.62$ and 500 ns for $M_c = 0.24$ was chosen in order to reduce the number of particles which leave the laser sheet owing to the out-of-plane velocity component of the particles. Laser optics (i.e. a combination of a cylindrical lens and a focusing lens) are used to form a laser sheet about 300 μm thick at the imaging area in the test section.

Scattering from the particles in the imaging area is collected from the direction normal to the laser sheet plane by an unintensified high-resolution (2000×2000 pixels) CCD camera (Kodak Megaplus 4.2). The camera is equipped with either Nikon 105 or 200 mm focal length macro lenses typically set to $f/11$–16. For taking plan-views, where the light sheet is set in the (x, z)-plane (see figure 2), the laser light sheet and the CCD camera are turned by 90° around the wind-tunnel free-stream axis, i.e. x-coordinate. Doubly exposed 8-bit grey-scale digital images from two separate pulses are captured by this camera at a frame rate of 1.7 Hz, then analysed by means of a two-dimensional fast Fourier transform (FFT)-based autocorrelation technique using commercial PIV software (TSI, INSIGHT NT Version 1.32). Centre and data peaks in the autocorrelation plane are localized using a Gaussian curve fit, which was chosen through the performance comparison among other peak search algorithms such as parabolic and Whittaker. Physically wrong vectors included in the processed vectors are omitted through range, angle and consistency filters, as described in detail by

Urban (1999). With an image size of 33–49 mm square in physical dimension on the imaging plane, spatial resolutions ranging from 1.3 to 1.9 mm are attained when using an interrogation region size of 80 pixels square. This relatively large interrogation spot size was adopted to reduce missing vectors in low-seeding-density regions in the shear layer and invalid vectors caused by noise and other error sources. In most vector maps presented below, the velocity vectors with 50% overlap between adjacent interrogation spots are shown.

In order to keep a minimum displacement (typically 5 pixels) required for the auto-correlation vector-processing algorithm using a short pulse separation, it is necessary to insert a rotating mirror between the camera lens and the imaging area in the higher M_c case to add a positive bias to the streamwise velocity. On the other hand, the mirror was not required for the lower-compressibility case since the turbulence intensity is lower than that of the higher M_c case, allowing a longer time separation.

The seed particle size of TiO_2 used in this experiment was measured in the present flow facility by Urban & Mungal (1997) by measuring the characteristic time of particles passing through an oblique shock. The results showed that the effective particle diameter in the test section is 0.4 μm. If the fluid characteristic time for large-scale motion, τ_f, is defined by $\delta/\Delta U$ where δ and ΔU denote shear-layer thickness in the test section and velocity difference between the two streams, respectively, corresponding Stokes number St defined by the ratio of particle to large-scale fluid characteristic time ($\equiv\tau_p/\tau_f$) is about 0.06 for the higher M_c case. Samimy & Lele (1991) conducted an investigation on an effect of slip velocity (i.e. velocity difference between the fluid and particles laden in the fluid) on velocity measurement accuracy of LDV and PIV. Their finding on an acceptable Stokes number guarantees that the velocity measurement error caused by the slip velocity is well below 1% for this value of St.

Ensemble averages of flow velocities and turbulence statistical quantities are derived from an ensemble of instantaneous velocity field data based on about 100 instantaneous images. In order to include a sufficient number of vectors to yield converged transverse (or spanwise) profiles of the derived values, vectors in the range of $x \pm 1$ cm at the same transverse (or spanwise) location are also used in the averaging process, leading to more than 2000 realizations at any point on the profile. Validity of the streamwise averaging was confirmed by comparing the streamwise-averaged data and non-averaged data, showing negligible differences within the accuracy of the present measurement. Only images with more than 94% vector yield are included for the averaging because low-yield images tend to include erroneous vectors. All missing vectors during the vector processing and validation are interpolated by a simple iterative Laplace interpolation scheme.

Uncertainty in the present PIV measurements was evaluated for instantaneous velocity, average velocity and turbulence statistical properties. In a detailed study of interrogation accuracy in PIV, Prasad *et al.* (1988) concluded that uncertainty for each instantaneous velocity vector is equal to approximately one-tenth of the particle image diameter when particle images are well resolved during digitization. This uncertainty is caused by the error in the displacement peak search process. Since, in this study, the particle diffraction-limited spot size is 40 μm, which corresponds to 4.4 times the CCD pixel size (9 μm), the particle image is judged to be well resolved according to the criteria, $d_{image}/d_{pixel} \geqslant 4$. Considering the average velocity of the high-speed and low-speed free streams as the representative flow velocity in the shear layer, the particle image displacement on the CCD array is 44 and 73 μm for $M_c = 0.62$ and 0.24 conditions, respectively. Therefore, for each instantaneous vector, the measurement uncertainty (2σ level) including the peak search error (i.e. 4.0 μm) and other major

error sources such as the time separation error and the velocity gradient error in an interrogation spot, is calculated to be 9.6% and 5.9% in total for $M_c = 0.62$ and 0.24, respectively. Uncertainty of average velocity and turbulence properties was evaluated, following the uncertainty evaluation method for measured statistical quantities by Bruun (1995). The resulting uncertainty for non-dimensionalized average velocity ($\langle u \rangle / \Delta U$, $\langle v \rangle / \Delta U$, and $\langle w \rangle / \Delta U$), turbulence intensity ($\sigma_u / \Delta U$, $\sigma_v / \Delta U$, and $\sigma_w / \Delta U$), and Reynolds stress ($\langle u'v' \rangle / \Delta U^2$ and $\langle u'w' \rangle / \Delta U^2$) is evaluated to be less than 0.0085, 0.0043 and 0.0011, respectively, when more than 1600 realizations at a point on transverse or spanwise profiles are used in the statistical data processing.

The PIV-based turbulence statistical data for the non-mixing-enhanced planar compressible shear layers using the present facility and PIV setting were compared with some LDV-based results (e.g. Elliott & Samimy 1990; Goebel & Dutton 1991) by Urban & Mungal (2001). The quantitative comparison showed overall validity of the present PIV measurement for the turbulence statistical properties.

Further details of the system design, image acquisition and data processing are described extensively in Urban (1999).

2.4. *Planar laser Mie scattering (PLMS)*

For comparison of the various disturbance configurations in terms of effectiveness of the mixing enhancement, both shear-layer thickness δ and growth rate of the layer $\mathrm{d}\delta/\mathrm{d}x$ at the imaging station can be used as measures of performance. In order to measure these values considering spanwise variations, spatially resolved visualizations of the shear layer were conducted via the PLMS technique, where a panoramic side-view image covers a range of 15 cm in the streamwise extent.

Ethanol is added into only the low-speed stream to produce shear-layer images in the 'product formation' mode (Clemens & Mungal 1991). In this mode, evaporated ethanol in the ambient-temperature low-speed stream condenses in the shear layer upon mixing with the cold supersonic stream. Scattering from the condensed ethanol droplets illuminated by a laser sheet marks only the shear layer instantaneously. The laser sheet in side-view was set at both peak and valley positions of the centre disturbance to allow average thickness and growth rate considering spanwise variations of them. Based on an averaged image of 40 instantaneous images at the same test condition, the upper and lower edges of the shear layer where image intensity is equal to 5% of the maximum intensity at the same streamwise location are detected, yielding the shear-layer thickness. Two measured values at the peak and valley positions were averaged to estimate an overall growth rate as a mean value in the spanwise direction.

2.5. *Schlieren*

Schlieren pictures were obtained from the side by using a conventional schlieren set-up with a horizontally located knife edge. The details of this schlieren system are described by Island (1997). In this study, considering that the schlieren technique is less affected by optical access restrictions of the facility than PIV or PLMS, the results were used to examine variations of the shear-layer growth rate in the streamwise direction from just downstream of the splitter tip to the end of the test section. However, it should be noted that spanwise variations of density gradient are not captured by the schlieren technique. Using the average image based on the 40 instantaneous images, the visual shear-layer thickness, δ_{vis}, was measured manually by marking the upper and lower visual edges of the shear layer in the whole streamwise extent of the image.

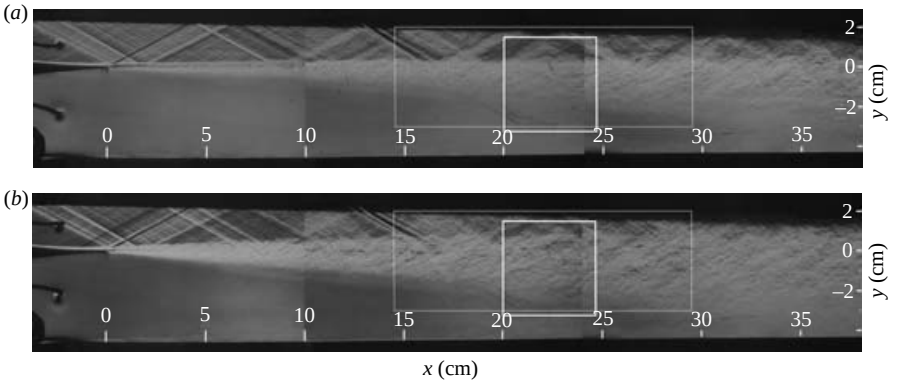

FIGURE 4. Instantaneous side-view schlieren photographs at $M_c = 0.62$: (*a*) no disturbances (Case 0) and (*b*) with disturbances (Case 3; $t/\delta_{99} = 18\%$). Thick and thin rectangles indicate imaging areas for side-view PIV and PLMS, respectively.

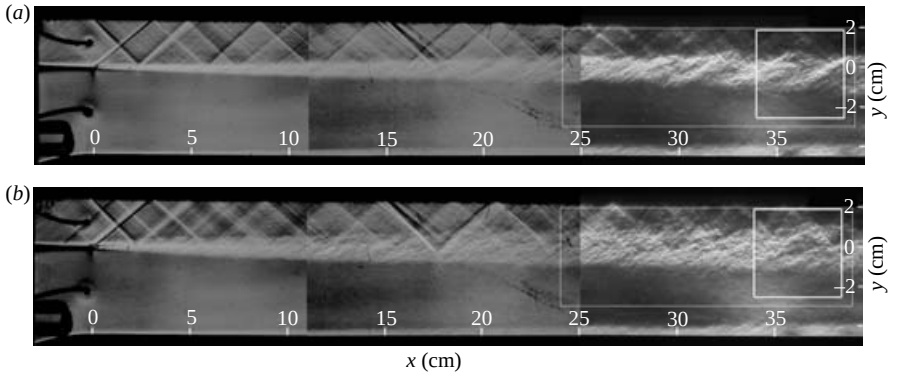

FIGURE 5. Instantaneous side-view schlieren photographs at $M_c = 0.24$: (*a*) no disturbances (Case 0) and (*b*) with disturbances (Case 3; $t/\delta_{99} = 18\%$). Thick and thin rectangles indicate imaging areas for side-view PIV and PLMS, respectively.

3. Results and discussion for optimum disturbance configuration

In this section, we present experimental data for Case 3, namely the optimum configuration employing five discrete equilateral triangles attached to the splitter tip with a thickness of $0.18\,\delta_{99}$ in comparison with the case with no disturbances, i.e. Case 0.

3.1. *Schlieren*

Figures 4 and 5 show comparisons of instantaneous panoramic schlieren photographs between cases without and with disturbances at $M_c = 0.62$ and 0.24, respectively. In the figures, the flow is from left to right with the high-speed stream at the top. Measurement areas for PLMS and PIV are also shown by rectangles. Weak shock trains originating from the splitter tip, the leading edge of the disturbances, wall mismatches, and so forth, can be seen in the high-speed (supersonic) stream, and it is clear from the photographs that they are weak, not affecting the shear-layer growth and its structure, since small deflections of the shear layer at the intersection of a relatively strong shock and shear layer are typically observed. The upper and lower wall pressure measurements in the present study show that an increase in the pressure

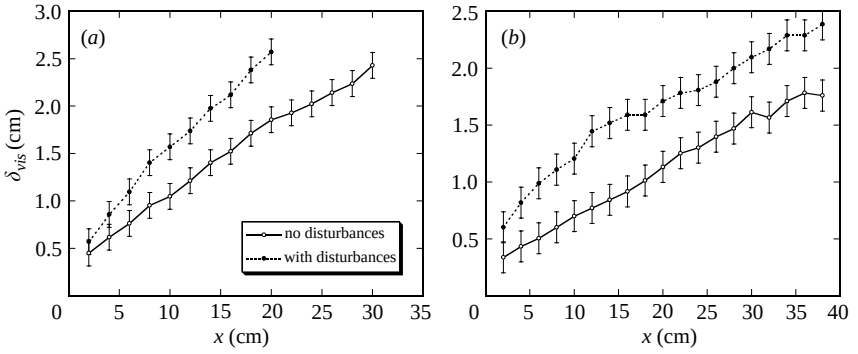

FIGURE 6. Visual shear-layer thickness (δ_{vis}) measured from schlieren photographs: (*a*) $M_c = 0.62$ and (*b*) $M_c = 0.24$. Data for Case 3 of $t/\delta_{99} = 18\%$ are shown as 'with disturbances'. Error bars of ± 0.14 cm indicate uncertainty in the manual measurement of δ_{vis}.

variation on the upper wall in the streamwise direction owing to the presence of the disturbances is only $\pm 2\%$ for the disturbed case, confirming this schlieren observation as well. Based on these results by schlieren, wall pressure measurement, PLMS and PIV as shown below, it can be concluded that the weak waves from the disturbances have little direct role in enhancing the mixing layer.

As already mentioned by Island *et al.* (1998), for both cases at $M_c = 0.62$, the shear layers grow almost linearly with streamwise distance from a virtual origin just upstream of the splitter tip to the downstream station ($x \approx 25$ cm) where the shear layer starts to interact with the boundary layers on the upper and lower walls, leading to a reduced growth rate. This observation is confirmed clearly in the shear-layer-thickness measurement result (figure 6*a*) based on the ensemble-average image. In the case with disturbances, the growth rate is about 45% higher than the no-disturbance case. Although this value might seem misleading because of spanwise averaging, this schlieren-based growth rate agrees well with the PLMS results showing about 50% increase as mentioned later in § 3.2.

Here, a question might arise whether this enhanced shear-layer growth rate will persist further downstream. In a PLMS study by Island *et al.* (1998) on the effect of spanwise disturbance size, it was inferred that the mixing-enhancement effect becomes maximum when the spanwise disturbance wavelength is comparable with the shear-layer thickness. Following this conclusion, it might be expected that the enhanced growth rate will decrease at the further downstream locations where the shear-layer thickness becomes much larger than the spanwise disturbance spacing. Streamwise-decreasing growth rate observed for the thickest disturbance as shown in § 4, where the shear-layer thickness is larger than the disturbance spacing, could validate this expectation.

As seen in figures 5 and 6(*b*) at $M_c = 0.24$, the growth rate stays nearly constant in the streamwise direction for the no-disturbance case as observed in many incompressible experiments in the past (e.g. Brown & Roshko 1974). On the other hand, the growth rate for the case with disturbances is higher than that of the no-disturbance case near the splitter tip (i.e. $x < 15$ cm), then reduced to the almost constant, undisturbed value at the further downstream regions, in contrast to the steady linear growth in the higher compressibility condition. The layer thickness itself at the downstream end of the measurement area ($x = 38$ cm) is about 30% thicker owing to the disturbances. This result indicates that at the nearly incompressible condition of $M_c = 0.24$, the

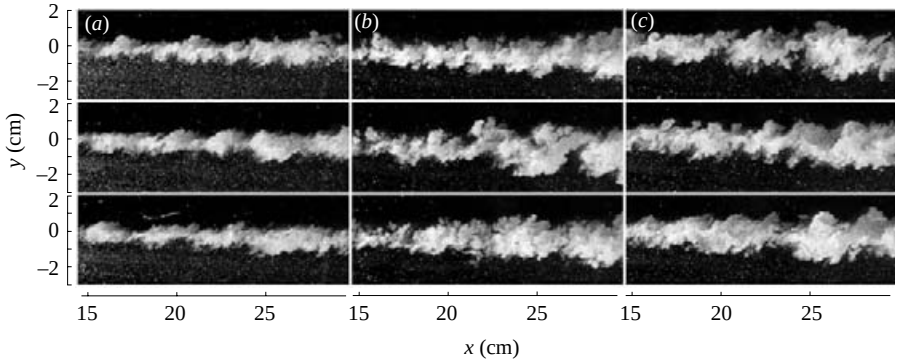

FIGURE 7. Instantaneous side-view PLMS images at $M_c = 0.62$: (*a*) no-disturbance case (Case 0; $z/B = 0$), (*b*) case with disturbances (Case 3; $t/\delta_{99} = 18\%$) at 'peak' position ($z/B = 0$) and (*c*) at 'valley' position ($z/B = -0.5$).

disturbances only have an initial effect for layer thickening, not affecting the growth rate in the fully developed region of the shear layer. Two-dimensional large-scale structures characterized by 'roller' and 'braid' can be observed in the no-disturbance case, as in other incompressible or nearly incompressible experiments (e.g. Brown & Roshko 1974; Clemens & Mungal 1995), whereas few two-dimensional structures are detected in the case with disturbances, at least initially. This could indicate that the streamwise structure generated by the disturbances interacts with the two-dimensional spanwise vortices initially, resulting in a highly three-dimensional structure, but the effect is lost further downstream. This observation will be discussed further with the PIV results in § 3.3.

3.2. *PLMS*

Figure 7 shows instantaneous side-view PLMS images for the cases with and without disturbances at $M_c = 0.62$. For the case with disturbances, the images were acquired at both peak and valley locations of the centre disturbance (i.e. $z/B = 0$ and -0.5, respectively), while the images were taken at the symmetry plane (i.e. $z/B = 0$) for the no-disturbance case. For each case, three independent images are chosen randomly from a large number of images to indicate temporal variation of the flow. As suggested by extensive PLMS measurements (Clemens & Mungal 1992*b*, 1995), the shear layer in the no-disturbance case does not show apparent two-dimensional structure while some images (e.g. the second image of the left-hand column) may contain somewhat two-dimensional features. In contrast to the no-disturbance case, two-dimensional structure is rarely observed for the disturbed case at both peak and valley locations, revealing the three-dimensional nature of the flow. Also, the shear layer for the case with disturbances seems more deformed owing to the stronger entrainment of the free streams into the shear layer than that for the case without disturbances. Another important finding is that the region with peak scattering intensity is located near the low-speed side edge of the shear layer for the disturbed case at the disturbance peak location, while it exists almost at the centre of the layer in the no-disturbance case. When examining the difference of the images at two spanwise locations, it is obvious that the shear layer at the valley position is higher (i.e. larger y) than that at the peak location.

To make the findings above more clear, the streamwise variation of average positions of the upper and lower edges (y_U and y_L) as well as peak intensity location, y_{peak},

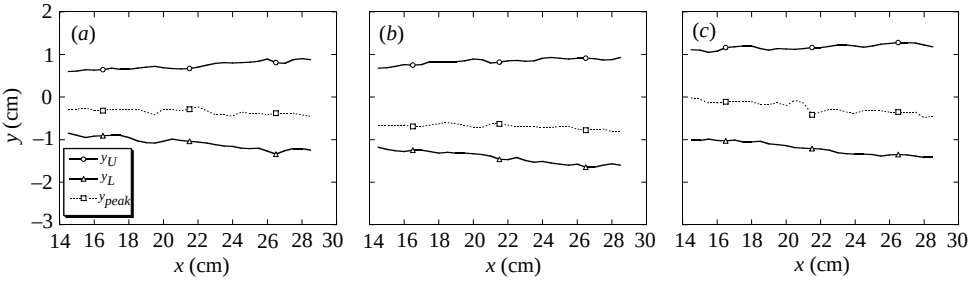

FIGURE 8. Average shear-layer shape from side-view PLMS results at $M_c = 0.62$: (*a*) no-disturbance case (Case 0; $z/B = 0$), (*b*) case with disturbances (Case 3; $t/\delta_{99} = 18\%$) at 'peak' position ($z/B = 0$) and (*c*) at 'valley' position ($z/B = -0.5$).

were calculated based on the averaged PLMS image as shown in figure 8. Average shear-layer thickness considering spanwise variation, δ_{ave}, is defined as follows:

$$\delta_{ave} = (\delta_P + \delta_V)/2 \quad \text{where } \delta = y_U - y_L. \tag{3.1}$$

Here, subscripts P and V denote a property measured at the peak and valley position of the triangular disturbance, respectively. As expected from the instantaneous PLMS images, average transverse position of the peak scattering intensity is apparently biased towards the lower edge of the shear layer for the case with disturbances at the disturbance peak position (figure 8*b*), whereas at the valley position of the disturbance, it is near the centre of the shear layer (figure 8*c*) as in the no-disturbance case (figure 8*a*). As will be shown in § 3.3, this coincides with the PIV result on the peak position of the turbulence intensity and Reynolds shear stress. Differences in the transverse position of the shear layer between the peak and valley positions are also confirmed in figures 8(*b*) and 8(*c*). For both disturbed and undisturbed cases, the upper and lower boundaries of the shear layer are close to straight lines, meaning that the shear-layer growth rate is almost constant in the observation area (Watanabe & Mungal 2000); this agrees with the schlieren test results (figure 6*a*). Average growth rate at the peak and valley positions is higher by about 50% than that for the no-disturbance case. It should be noted that the change of y_L in the streamwise direction is much larger than the change of y_U, indicating that mixing on the low-speed side of the layer is enhanced more effectively than on the high-speed side.

Figures 9 and 10 show corresponding PLMS results at $M_c = 0.24$ in the same formats as those for $M_c = 0.62$. Investigating the instantaneous images (figure 9), the well-organized roller-and-braid structure is evident for the no-disturbance case (figure 9*a*) as observed at the identical compressibility condition by PLMS (Clemens & Mungal 1995) or in incompressible conditions by shadowgraph (Brown & Roshko 1974). In contrast to the two-dimensional feature for the no-disturbance case, the shear layer for the disturbed case (figure 9*b*, *c*) shows diffused three-dimensional structure with stronger entrainment even at the nearly incompressible condition. Similar to $M_c = 0.62$, the line corresponding to the peak scattering intensity for the case with disturbances at the peak position is close to the low-speed stream. At this compressibility level, the peak intensity position even for the no-disturbance case is also slightly close to the lower edge. It should be noted that in this lower compressibility condition, the shear layer grows almost equally on both high- and low-speed sides in contrast to the greater growth on the low-speed side interface at $M_c = 0.62$.

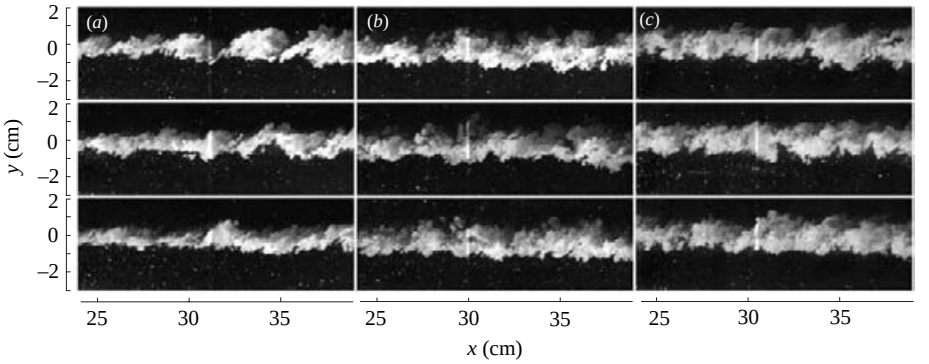

FIGURE 9. Instantaneous, side-view PLMS images at $M_c = 0.24$: (*a*) no-disturbance case (Case 0; $z/B = 0$), (*b*) case with disturbances (Case 3; $t/\delta_{99} = 18\%$) at 'peak' position ($z/B = 0$) and (*c*) at 'valley' position ($z/B = -0.5$).

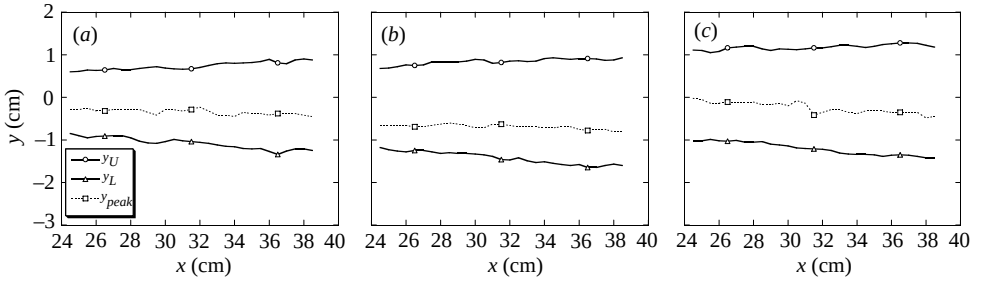

FIGURE 10. Average shear-layer shape from side-view PLMS results at $M_c = 0.24$: (*a*) no-disturbance case (Case 0; $z/B = 0$), (*b*) case with disturbances (Case 3; $t/\delta_{99} = 18\%$) at 'peak' position ($z/B = 0$) and (*c*) at 'valley' position ($z/B = -0.5$).

3.3. *PIV*

3.3.1. *Side-views*

In this section, we compare the side-view PIV results with no disturbances to those with disturbances at the higher compressibility condition, $M_c = 0.62$, to investigate the effect of the mixing enhancement on the velocity fields.

Figure 11 shows, in the left-hand column, a comparison of contours of instantaneous velocity magnitudes derived from side-view images. The figure also includes, in the right-hand column, corresponding velocity maps and vorticity contours in a convective frame. The spanwise location, z, of the laser light sheet was set at the 'peak' of the centre triangular disturbance or its 'valley'. Velocity vectors shown here are measured in a frame convecting at the convective velocity, U_c, defined in (1.2). This frame is introduced to see clearly the structure of the vortices embedded in the shear layers.

In the no-disturbance case (figure 11*a*(i)), thin layers with steep velocity gradients can be seen in the shear layer as reported in Urban & Mungal (2001). Two layers at interfaces with the high- and low-speed free streams are not necessarily observed for the present measurements, partly because the spatial resolution is about half of that of Urban & Mungal (2001), making capture of the thin layers more difficult. High-vorticity layers corresponding to the layers with steep transverse gradient of the streamwise velocity are seen in figure 11(*a*)(ii) since the term in the transverse gradient of the streamwise velocity, $\partial u/\partial y$, is dominant relative to the other term $\partial v/\partial x$ in

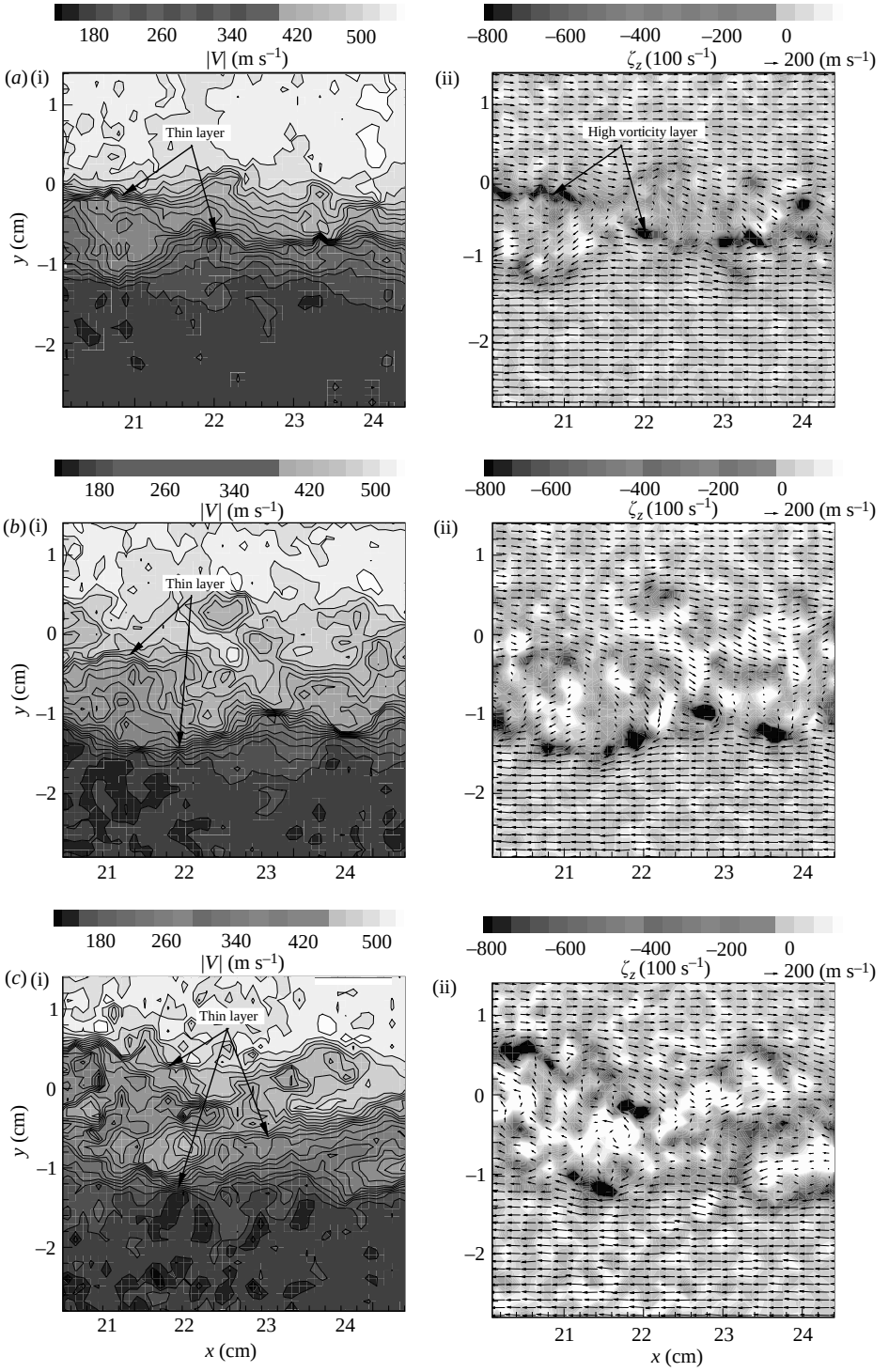

FIGURE 11. (i) Instantaneous velocity magnitude contours and (ii) velocity vectors and vorticity contours in a convecting frame at $M_c = 0.62$ (side-view): (*a*) no-disturbance case (Case 0), (*b*) case with disturbances at 'peak' and (*c*) case with disturbances at 'valley' (Case 3; $t/\delta_{99} = 18\%$). Velocity vectors in (ii) indicate velocity observed from a frame convecting at U_c.

the vorticity equation. The vortices in the shear layer are too small to span the whole thickness of the layer in contrast to the 'roller' and 'braid' structure dominant in incompressible shear layers. The vortices forming the thin layers do not appear as vortices in the frame convecting at U_c, indicating the vortices in the two layers are convecting with different speeds. This result is quantitatively consistent with the PIV measurement results for a weakly compressible shear layer ($M_c = 0.38$) by Olsen & Dutton (2003), who find differing convective velocity across the layer. These facts mean that a single convective velocity across the shear layer loses physical significance with increase in the compressibility of the shear layer (e.g. Elliott, Samimy & Arnette 1995).

In the case with disturbances (figure 11*b*, *c*), the shear layer is much thicker than that of the no-disturbance case. The shear layer cut by the plane including the peak of the centre disturbance is higher than that at the valley position, meaning that the shear-layer position is varying periodically in the spanwise direction according to the spacing of the disturbances. This wavy layer shape was also predicted by the PLMS results presented in figure 8(*b*, *c*). Thin layers with steep velocity gradients can also be seen in the enhanced case. In most images, two layers with the steep gradients are found near the upper- and lower-edge of the shear layer, often with the lower one being prominent. At the valley position, three layers are observed in some images as shown in figure 11(*c*)(i). In the region between the layers, vorticity is low or has an opposite sign (plus = white in figure 11*c*(ii)) from the sign of the main vortices (minus = black).

Figure 12 shows transverse profiles of (*a*, *b*) ensemble-average velocities $\langle u \rangle$ and $\langle v \rangle$, (*c*, *d*) turbulence intensities for streamwise and transverse velocity σ_u and σ_v, (*e*) anisotropy of turbulence σ_u/σ_v, (*f*) Reynolds stress $\langle u'v' \rangle$, and (*g*) vorticity around the spanwise coordinate ζ_z. Here, σ and $\langle\ \rangle$ denote a root-mean-squared value of a fluctuating property and an ensemble average, respectively, whereas a value with a prime means a fluctuation from the mean value. The transverse coordinate, y, is normalized by the shear-layer thickness in the no-disturbance case, δ_{nd}, with its origin set to the centre location between the upper and lower edges of the layer, $y_{cl}(=[y_U + y_L]/2)$. The velocities and turbulence quantities in figure 12 are normalized by using the velocity difference between the high- and low-speed streams, $\Delta U(\equiv U_1 - U_2$, where U_1 and U_2 denote the high- and low-speed free-stream velocities, respectively). The shear-layer thickness as a reference length is taken to be the distance between transverse locations where the mean streamwise velocity is equal to $U_1 - 0.05\Delta U$ and $U_2 + 0.05\Delta U$.

As observed in figure 12(*a*), the streamwise velocity profile in the case of no disturbances shows a smooth error-function-like distribution. On the other hand, the velocity profile has triple inviscidly unstable inflection points in the case with disturbances at both peak and valley positions of the centre triangular disturbance. Since these inflection points can be found by averaging only 20 images and the characteristic profile does not change significantly by increasing the number of images for averaging, this suggests that this result is not an effect of insufficient statistical convergence. Although velocity profiles like this have been reported in previous works on incompressible mixing layers (Nygaard & Glezer 1991; Foss & Zaman 1999), the characteristic profile seems rare in compressible shear layers as far as we know. At the valley position, the velocity profile has more distinct triple inflection points than at the peak position, and the streamwise velocity changes almost linearly in the shear layer in the transverse direction. The two thin vortex layers observed in the instantaneous velocity fields (figure 11*b*, *c*) correspond to the high-velocity gradient positions at the top and bottom inflection points in the transverse profile. Also, the transverse position of the shear

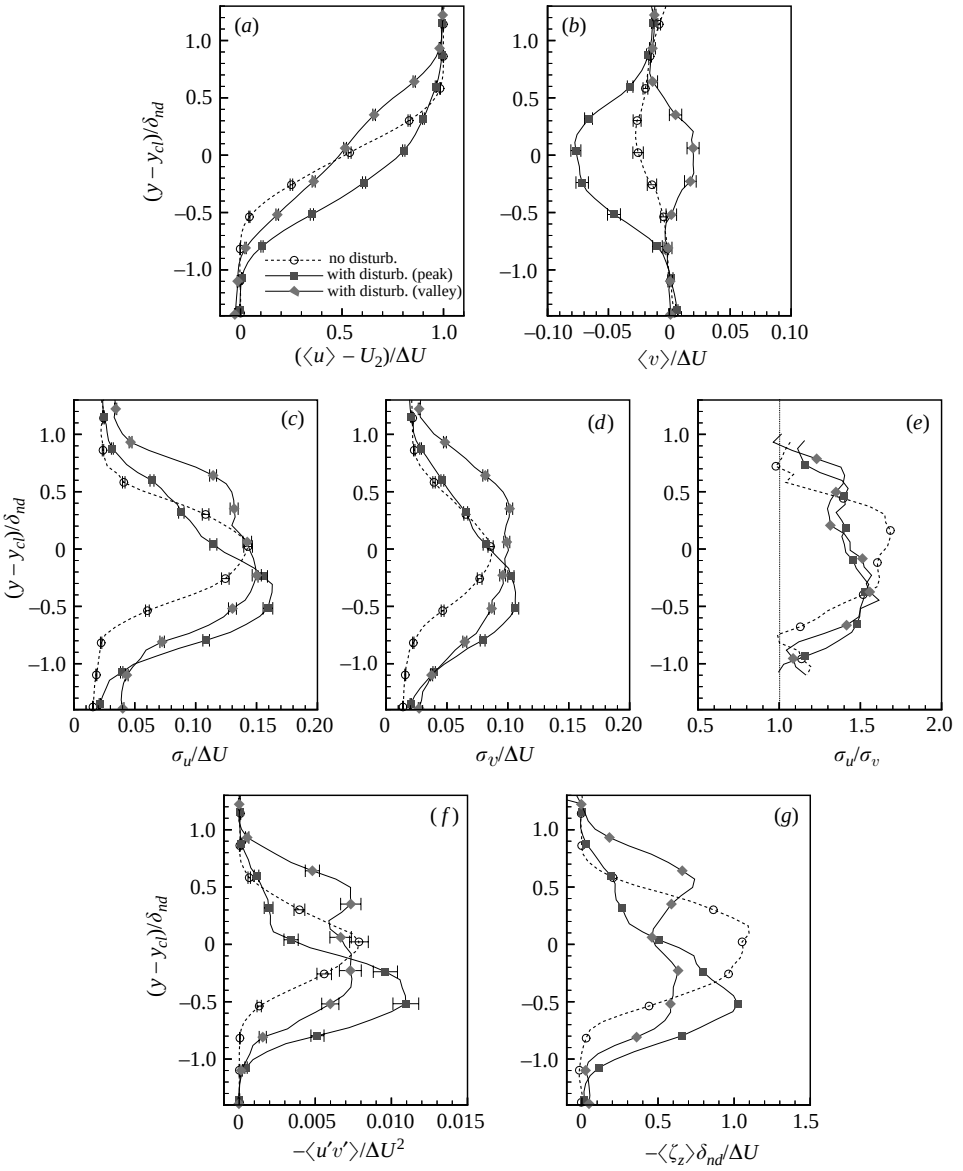

FIGURE 12. Transverse profiles of average velocity and turbulence statistic quantities at $M_c = 0.62$: (*a*) average streamwise velocity, (*b*) average transverse velocity, (*c*) streamwise turbulence intensity, (*d*) transverse turbulence intensity, (*e*) anisotropy, (*f*) Reynolds stress and (*g*) vorticity around the spanwise coordinate. 'With disturb.' indicates data for Case 3 of $t/\delta_{99} = 18\%$. Error bars denote 2σ uncertainty intervals (i.e. 95% confidence intervals).

layer at the valley is higher by 10% of the shear-layer thickness and slightly thicker than that at the peak, coinciding with the PLMS measurements.

Ensemble-average transverse velocity, $\langle v\rangle$, is nearly zero (flow angle less than 1.5°) even in the shear layer for the no-disturbance case (figure 12*b*). On the other hand, $\langle v\rangle$ has non-zero values in the shear layer in the case with disturbances. Maximum flow angle relative to the x-coordinate is 3.5° at around $y = y_{cl}$ at the peak position.

The sign of $\langle v \rangle$ at the peak being opposite to that at the valley suggests an existence of a streamwise vortex generated by a disturbance element.

As expected from the velocity profile with the triple inflection points, the turbulence intensities and Reynolds stress (figure 12*c–d*, *f*) have 'bumps' corresponding to the top inflection point in addition to the peaks corresponding to the bottom, dominant inflection point. The linear velocity profile in the shear layer at the valley causes flat-top profiles of the turbulence quantities at the middle of the layer. Peaks of the streamwise and transverse turbulence intensities, σ_u and σ_v, respectively, for the case with disturbances are greater than those in the no-disturbance case, resulting in a higher peak of Reynolds stress. This means that the transport of x-momentum across the shear layer is enhanced by the disturbances. Regarding measurement accuracy, it should be noted that the peak value of the Reynolds stress (a crucial measure in the validation of turbulence measurements) in the present measurements agrees with that for the PIV results with twice as much spatial resolution (Urban & Mungal 2001) and that for several extensive LDV studies (e.g. Elliott & Samimy 1990; Goebel & Dutton 1991) well within the uncertainty level between those experimental results. This guarantees that the relatively low spatial resolution achieved in the present measurements allows us to discuss turbulence properties quantitatively.

In the shear layer, Reynolds normal stress anisotropy, σ_u/σ_v (figure 12*e*), is about 1.4 in the disturbed case and 1.7 in the no-disturbance case, indicating that the enhancement technique has the additional effect of alleviating the increased anisotropy in high compressibility conditions observed by Goebel & Dutton (1991), Gruber *et al.* (1993) and Urban & Mungal (2001). Considering that the anisotropy seems to act to suppress the growth rate of the shear layer with a nearly constant σ_u (e.g. Goebel & Dutton 1991), this could be a substantial effect promoting the mixing enhancement.

The normalized vorticity around the spanwise coordinate, $-\langle \zeta_z \rangle \delta_{nd}/\Delta U$ (figure 12*g*), has similar profiles to the Reynolds stress since both quantities are mainly contributed by the transverse velocity gradient, $\partial u/\partial y$. At the valley, two peaks of the vorticity are obvious as expected from the instantaneous vorticity fields as shown in figure 11(*c*)(ii). It should be noted that the peak value of the vorticity for the disturbed case is slightly lower than that for the no-disturbance case since the velocity gradient decreases in general with the increased thickness of the layer at the constant velocity difference between the high- and low-speed streams for the case with disturbances.

3.3.2. *Plan-views*

In this section, the plan-view PIV results with the laser sheet parallel to the (x, z)-plane are presented for the cases with and without disturbances at $M_c = 0.62$.

Figure 13 shows instantaneous velocity magnitude contours in the left-hand column while the right-hand column presents instantaneous velocity vectors and vorticity contours in a convecting frame. Since the convective velocity given by (1.2) seems to lose its physical significance at the higher compressibility condition as shown in figure 11, a frame convecting at a spanwise-averaged mean streamwise velocity, $(\langle u_P \rangle + \langle u_V \rangle)/2$, is adopted in the plan-view velocity field investigation to show clearly the vortex structure at a transverse position of interest. The transverse station for the plan-view in this figure is chosen to be the station where the following relation is met: $\langle u_P \rangle = U_2 + 0.6\Delta U$. We use this definition to compare the plan-view data for the cases with and without disturbances on a reasonable basis. This location of $0.6\Delta U$ is at the middle of the shear layer, a little lower than the peak location of $\langle v \rangle$ (i.e. the core location of the streamwise vortices) for the disturbed case.

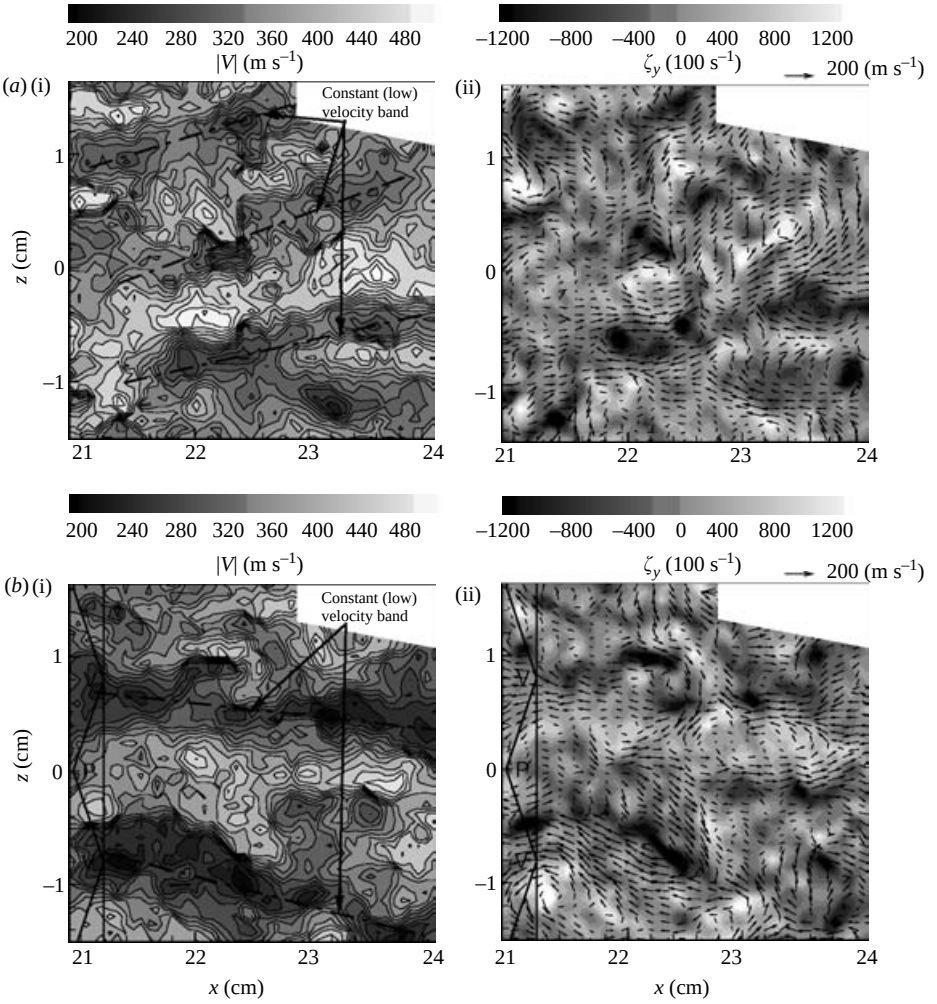

FIGURE 13. (i) Instantaneous velocity magnitude contours and (ii) velocity vectors and vorticity contours in a convecting frame at $M_c = 0.62$ (plan-view): (*a*) no-disturbance case (Case 0), (*b*) case with disturbances (Case 3; $t/\delta_{99} = 18\%$). Measurement plane is set at the transverse position where $\langle u_P \rangle = U_2 + 0.6\Delta U$. Velocity vectors in (ii) indicate velocity observed from a frame convecting at a spanwise-averaged mean streamwise velocity, $(\langle u_P \rangle + \langle u_V \rangle)/2$. Triangles in (*b*) denote the spanwise spacing and location of the disturbances.

In the no-disturbance case (figure 13*a*), bands of constant velocity magnitude are seen in the majority of the instantaneous images. They are aligned in a nearly streamwise direction while some bands have angles up to 30° to the free-stream direction. It should be noted that they seem to be located periodically in the spanwise direction with an interval of about 10 mm, or 80% of the local layer thickness. Since these bands are not seen in the ensemble average of streamwise velocity, $\langle u \rangle$, in plan-view (to be shown in figure 14*a*), it is concluded that they are not fixed to a certain spanwise position, moving freely about in the spanwise direction. The spanwise interval is close to half of the disturbance width, which is possibly related to the present disturbance spacing of 16 mm having an enhancement effect superior to larger or smaller spacings (Island *et al.* 1998). As shown in figure 13(*a*)(ii), it should be noted

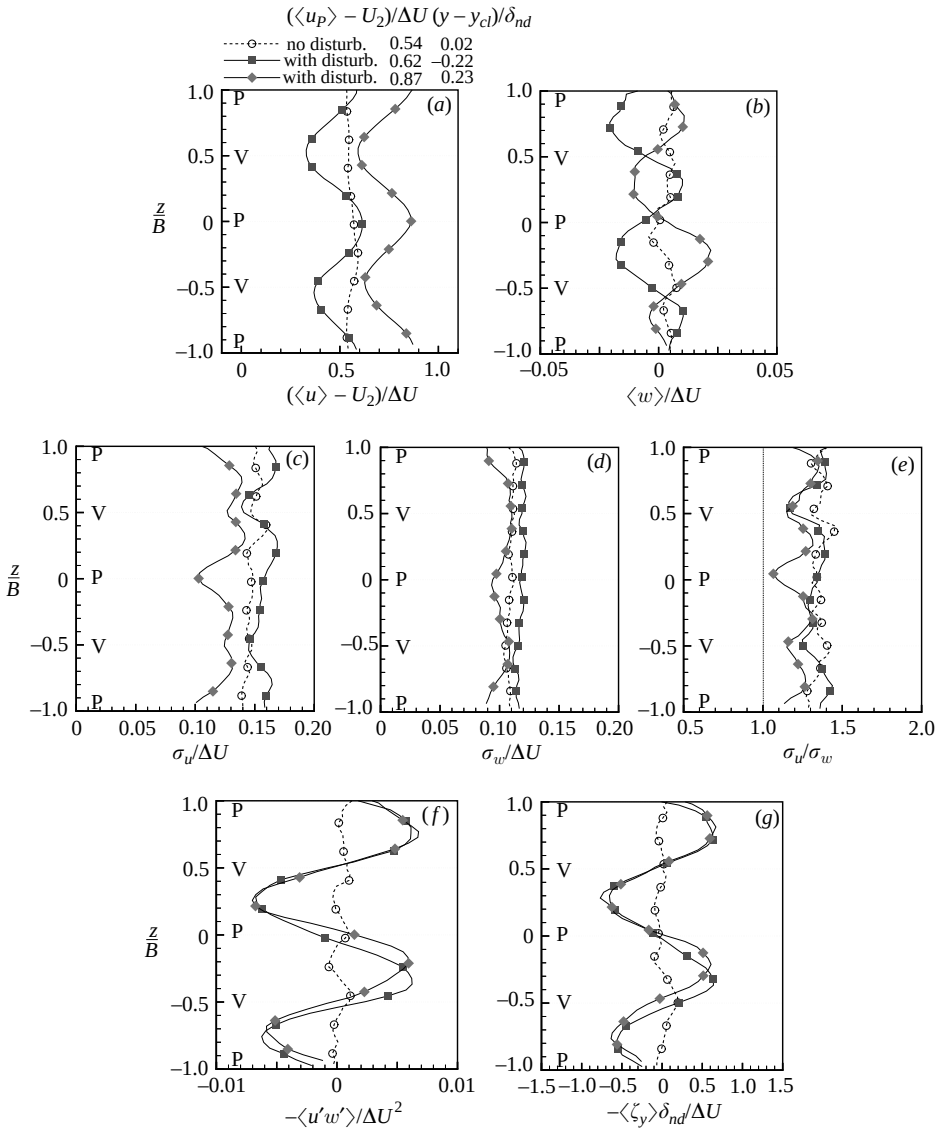

FIGURE 14. Spanwise profiles of ensemble-averaged velocity and turbulence statistical quantities at $M_c = 0.62$: (*a*) average streamwise velocity, (*b*) average transverse velocity, (*c*) streamwise turbulence intensity, (*d*) transverse turbulence intensity, (*e*) anisotropy, (*f*) Reynolds stress and (*g*) vorticity around the transverse coordinate. 'With disturb.' indicates data for Case 3 of $t/\delta_{99} = 18\%$. 'P' and 'V' denote spanwise location of the peak and valley of the disturbance, respectively. The spanwise coordinate z is normalized by the disturbance width B (= 1.6 cm).

that the peak level of the vorticity is comparable to that in side-view where a mean shear exists owing to the velocity difference between the free streams. Since the vorticity fields consist of complicated interlinking vortices, it is difficult to find a common character.

In the case with disturbances (figure 13*b*(i)), the bands of constant velocity magnitude observed above are fixed to the spanwise position of the peaks and valleys of the disturbances, while there are some variations of interval and angle to the free stream

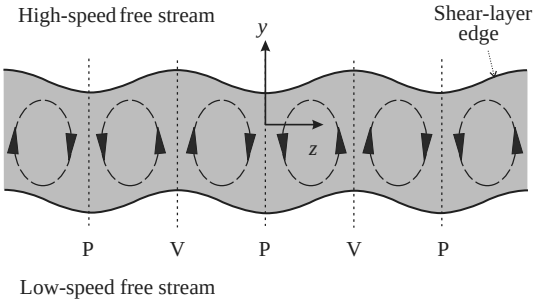

FIGURE 15. Schematic of streamwise vortices introduced into shear layer by triangular disturbances at $M_c = 0.62$. This is viewed from upstream. 'P' and 'V' denote locations of the peaks and valleys of the disturbances, respectively.

in the instantaneous velocity fields. At the peak position, the velocity magnitude has a maximum while it has a minimum at the valley position. As shown in figure 13(*b*)(ii), the peak value of vorticity is comparable to that in side-view as in the no-disturbance case.

Figure 14 shows spanwise profiles of (a, b) ensemble-average streamwise and spanwise velocities $\langle u \rangle$ and $\langle w \rangle$, (c, d) streamwise and spanwise turbulence intensities σ_u and σ_w, (e) anisotropy σ_u/σ_w, (f) Reynolds stress $\langle u'w' \rangle$, and (g) vorticity around the y-coordinate ζ_y. The spanwise coordinate, z, is normalized by the width of the disturbances, B (=16 mm). This figure contains plan-views for the disturbed case at two transverse locations in the shear layer. From the data for $\langle v \rangle$ in side-view (figure 12*b*), the induced streamwise vortices were expected to exist between the two transverse locations. On the other hand, plan-view for the no-disturbance case was acquired at only one location.

In the case with no disturbances, average streamwise velocity, $\langle u \rangle$ (figure 14*a*), is almost constant in the spanwise direction within a variation of $\pm 3\% \Delta U$. The other quantities (figure 14*b–g*) are nearly constant as well, with small variations, indicating absence of stationary streamwise structures for the no-disturbance case. In the case with disturbances, the average streamwise velocity $\langle u \rangle$ has maximum values at the peak position while having minimum values at the valley position. Sinuous velocity variations are observed at both transverse locations across the layer. This periodic streamwise velocity variation means existence of inflection points in the spanwise direction in addition to the triple inflection points across the shear layer shown in figure 12(*a*). These transverse and spanwise inflection points could synergistically enhance inherent shear layer instability, leading to an effective mixing enhancement.

In figure 14(*b*), it is found that average spanwise velocity, $\langle w \rangle$, is nearly zero at the peak and valley positions, having maximum and minimum values between a peak and a valley. The phase is opposite between the lower station (transverse position of $0.62\Delta U$) and the higher station ($0.87\Delta U$). Three-dimensionally interpreting the data of $\langle u \rangle$ and $\langle w \rangle$ in plan-view together with the data of $\langle u \rangle$ and $\langle v \rangle$ obtained in side-view (figure 12a, b) clearly reveals the existence of a pair of counter-rotating streamwise vortices generated by an individual disturbance, as sketched in figure 15. It is surprising that streamwise vortices generated by the triangular-shaped disturbances of sub-boundary-layer thickness still survive in a stationary condition down to the fully developed region of the shear layer, indicating strong stability of the vortices embedded in the compressible shear layer. Although the rotating direction of these vortices is opposite to those of vortices induced by upward-deflected triangular tabs

or corrugated splitter tips applied for incompressible shear layers (e.g. Foss & Zaman 1999), the present result is considered reasonable since the flow around the triangular disturbance on the splitter tip should be similar to the three-dimensional shock-boundary-layer interaction flow field around a fin in a supersonic stream with a resulting horseshoe vortex. In addition, oil flow test results on the upper surface of the splitter plate (not shown here) confirm this flow similarity. Each streamwise vortex locates between peak and valley positions of a disturbance, and induces a downward flow at a peak and an upward flow at a valley. The downward and upward flows deflect the cross-sectional shape of the shear layer, resulting in a wavy geometry in the spanwise direction (figure 15). It is believed that this spanwise deformation of the layer causes the spatially periodic inflection points in the streamwise velocity profile in the spanwise direction (figure 14*a*).

Although the spanwise variation of the streamwise turbulence intensity, σ_u, is relatively small, it appears to have peak values at the streamwise vortex core positions, while having local minimum values at the peak and valley positions (figure 14*c*). On the other hand, variation of the spanwise turbulence intensity, σ_w, is less than that of σ_u as seen in figure 14(*d*). Reynolds normal stress anisotropy (figure 14*e*) based on the plan-view has a spanwise trend similar to that for σ_u since the spanwise variation of σ_w is small. The anisotropy σ_u/σ_w for the no-disturbance case, which is assumed to be nearly equal to its peak value at the transverse location close to the centre of the shear layer, is about 1.3, almost agreeing with the peak value in the three-dimensional LDV measurements by Gruber *et al.* (1993) at a higher compressibility condition ($M_c = 0.80$), indicating weak compressibility effects on σ_w as well as σ_u. Although it is difficult to evaluate the variation of σ_u/σ_w across the shear layer based on the present limited measurements, the fact that the average anisotropy at two transverse locations for the disturbed cases is smaller than that for the no-disturbance case could infer that the present mixing enhancement technique has the effect of reducing the anisotropy in terms of streamwise and spanwise velocity fluctuation components (σ_u/σ_w) as well as the favourable (i.e. reducing) effect on the anisotropy in terms of streamwise and transverse components (σ_u/σ_v).

As shown in figure 14(*f*, *g*), in the case with disturbances, Reynolds stress $\langle u'w' \rangle$ and vorticity around the transverse coordinate have similar sinuous spanwise variations, as expected from the spanwise variation of $\langle u \rangle$ (figure 14*a*). The peak value of $\langle u'w' \rangle$ is 60% of that of $\langle u'v' \rangle$, indicating the significance of the x-momentum transport in the spanwise direction when compared with the original transport across the shear layer.

3.3.3. *Compressibility effect*

In this section, to examine the compressibility effect on the mixing enhancement, the side-view data at $M_c = 0.24$ for the no-disturbance (Case 0) and disturbed cases (Case 3 of $t/\delta_{99} = 18\%$) are presented as counterparts to the results at the higher compressibility condition ($M_c = 0.62$) which have been presented in § 3.3.1.

Figure 16 shows a comparison of the instantaneous velocity magnitude contours in side-view between the cases with and without disturbances. The figure also includes the corresponding velocity vector map in a frame convecting at U_c and vorticity contours. The corresponding results at $M_c = 0.62$ were shown in figure 11. As shown in figure 16(*a*)(i), the velocity gradient in the no-disturbance case is more gentle than that at the higher compressibility case (figure 11*a*(i)). The organized 'roller' and 'braid' structures characterized in the incompressible shear layers are apparent (16*a*(ii)) where a single large roller spreads through the whole shear layer thickness. The fact that the rollers look stationary in a frame convecting at U_c supports the validity of the

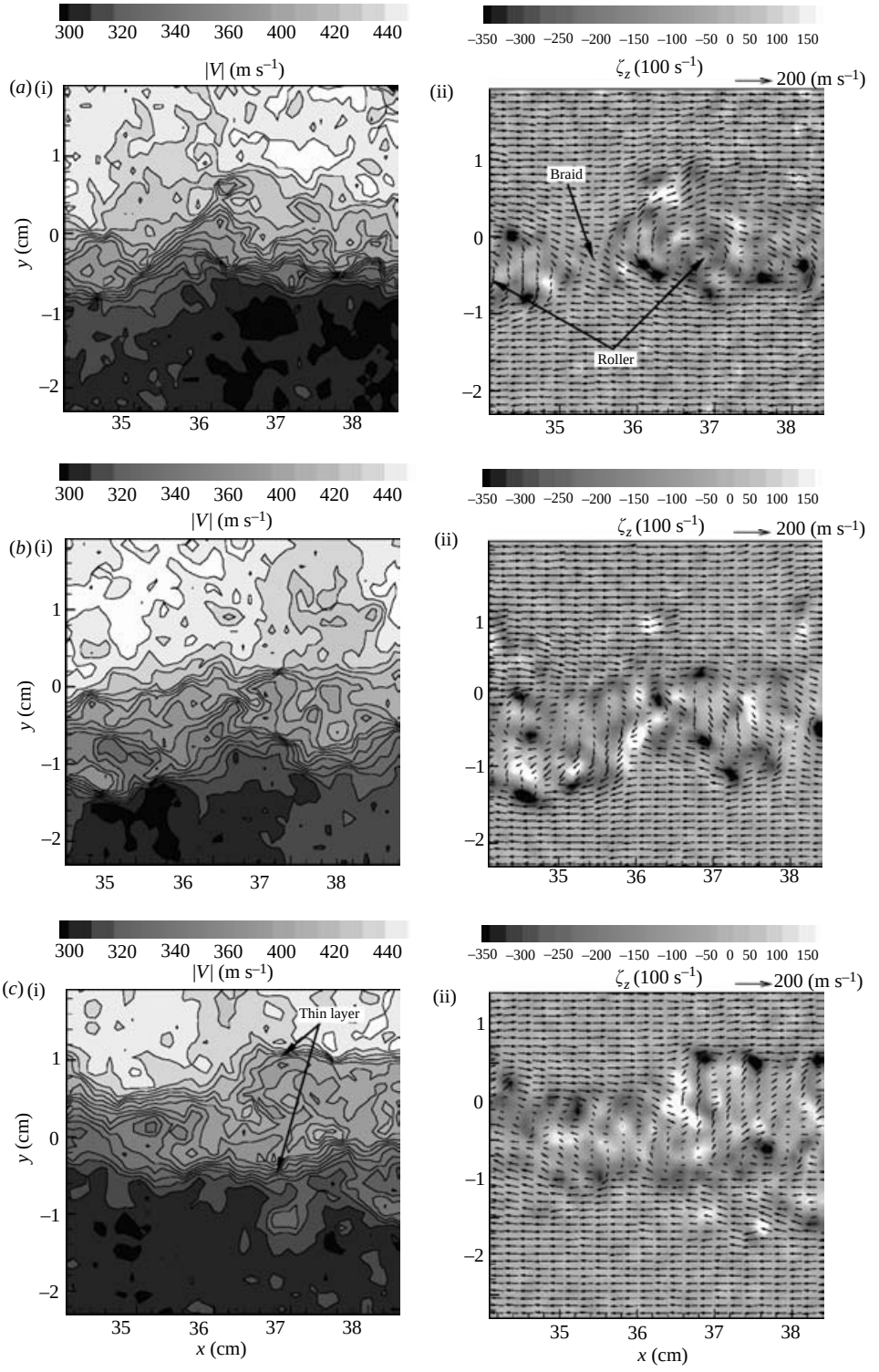

FIGURE 16. (i) Instantaneous velocity magnitude contours and (ii) velocity vectors and vorticity contours in a convecting frame at $M_c = 0.24$ (side-view): (*a*) no-disturbance case (Case 0), (*b*) case with disturbances at 'peak' and (*c*) case with disturbances at 'valley' (Case 3; $t/\delta_{99} = 18\%$). Velocity vectors in (ii) indicate velocity observed from a frame convecting at U_c.

concept of a single convective velocity (e.g. Bogdanoff 1983) in low compressibility conditions.

In the case with the disturbances (figure 16*b*, *c*), the organized large-scale rollers are not found in most images. In some images such as figure 16(*c*), two thin layers similar to those at $M_c = 0.62$ are apparently observed. On the other hand, it should be noted that the spanwise rollers can definitely be seen in some of the images, indicating that the streamwise structures generated by the disturbances are disorganized downstream, and eventually, the intrinsic two-dimensional structures appear again. This supports the schlieren results (figure 6*b*), which show almost identical growth rate in the fully developed region for both cases with and without disturbances. It is inferred that the two-dimensional structure dominant in low compressible shear layers can suppress the effect of the present mixing enhancement which introduces streamwise vortices whose axes are orthogonal to the spanwise rollers. On the other hand, in higher compressibility conditions, the two-dimensional structure changes to a highly three-dimensional oblique or streamwise structure (Clemens 1991, and figure 13*a*). If the nearly streamwise structures do exist by nature in the compressible shear layer, the streamwise vortices generated by the present triangular disturbances could enhance the original structure, leading to effective mixing enhancement.

Figure 17 shows transverse profiles of average velocities, turbulence intensities, Reynolds stress and vorticity at $M_c = 0.24$. The corresponding results at $M_c = 0.62$ were shown in figure 12. Generally speaking, all data at $M_c = 0.24$ for the case with disturbances show qualitatively similar results to those at $M_c = 0.62$. However, two interesting effects of compressibility can be observed. (i) In the disturbed case, the lower edge position relative to the velocity profile for the no-disturbance case is higher than that at $M_c = 0.62$ while the higher edge position is almost identical. From this observation, it is inferred that the low-speed-side preference of the mixing (growth) enhancement at the higher compressibility condition does not exist at the lower compressibility condition. (ii) In the no-disturbance case, turbulence intensities (especially, transverse component) and Reynolds stress at $M_c = 0.24$ are higher than those at $M_c = 0.62$ as previous workers have reported in their experimental studies (Goebel & Dutton 1991; Urban & Mungal 2001) or in numerical analysis (Freund *et al.* 2000). Notably, Reynolds normal stress anisotropy is weaker (i.e. $\sigma_u/\sigma_v = 1.4$) at this low compressibility condition than its counterpart ($\sigma_u/\sigma_v = 1.7$) at $M_c = 0.62$. On the other hand, in the case with disturbances at $M_c = 0.24$, peak values of these quantities as well as the anisotropy are almost equal to the values at $M_c = 0.62$, resulting in small differences in the peak values between the no-disturbance and disturbed cases. This observation reveals a reason for the ineffective mixing enhancement at the lower compressibility case which is observed in the schlieren investigation (§ 3.1).

4. Results and discussion for disturbance configuration variations

In this section, the results for the configuration variations of the disturbances for mixing enhancement at $M_c = 0.62$ are compared. Then, the results for all the configurations are comprehensively correlated with respect to selected parameters; finally, the compressibility effects are discussed again.

4.1. *Effects of disturbance thickness*

Figure 18 compares transverse profiles of average velocities, vorticity and turbulence quantities for different disturbance thicknesses, t, at $M_c = 0.62$. It is clear that the shear-layer thickness increases with increase in the disturbance thickness (figure 18*a*).

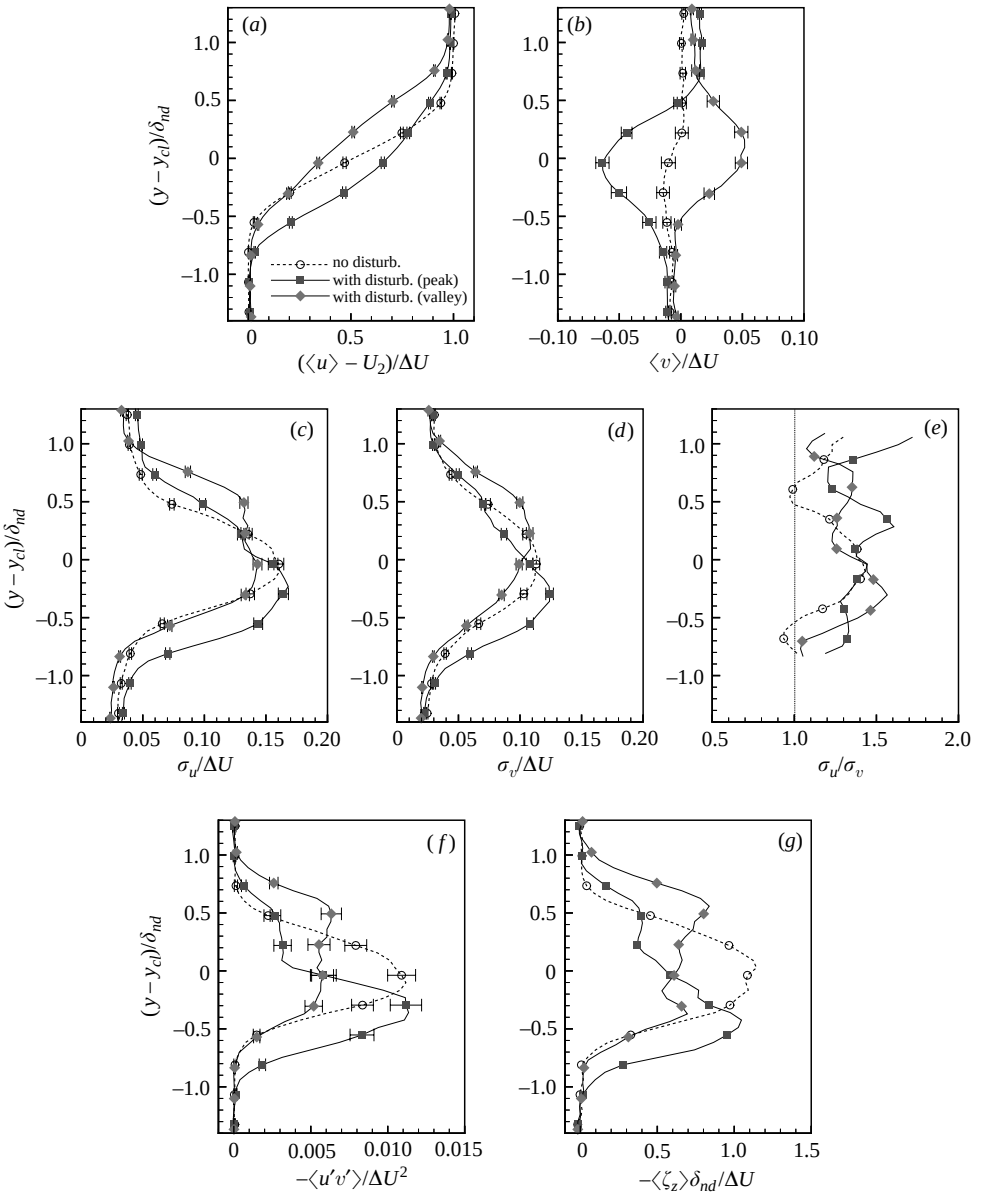

FIGURE 17. Transverse profiles of average velocity and turbulence statistical quantities at $M_c = 0.24$: (*a*) average streamwise velocity, (*b*) average transverse velocity, (*c*) streamwise turbulence intensity, (*d*) transverse turbulence intensity, (*e*) anisotropy, (*f*) Reynolds stress and (*g*) vorticity around the spanwise coordinate. 'With disturb.' indicates data for Case 3 of $t/\delta_{99} = 18\%$. Error bars denote 2σ uncertainty intervals (i.e. 95% confidence intervals).

The velocity profiles with triple inflection points can be observed for both disturbed cases while the upper inflection point at the peak position becomes evident with increase in the disturbance thickness. Considering that the shear layer for the case of $t/\delta_{99} = 37\%$ is thicker than that for the case of $t/\delta_{99} = 18\%$, it is inferred that the characteristic velocity profile is an indication of an effective mixing-enhancement technique. The strength of the streamwise vortices which is represented by the

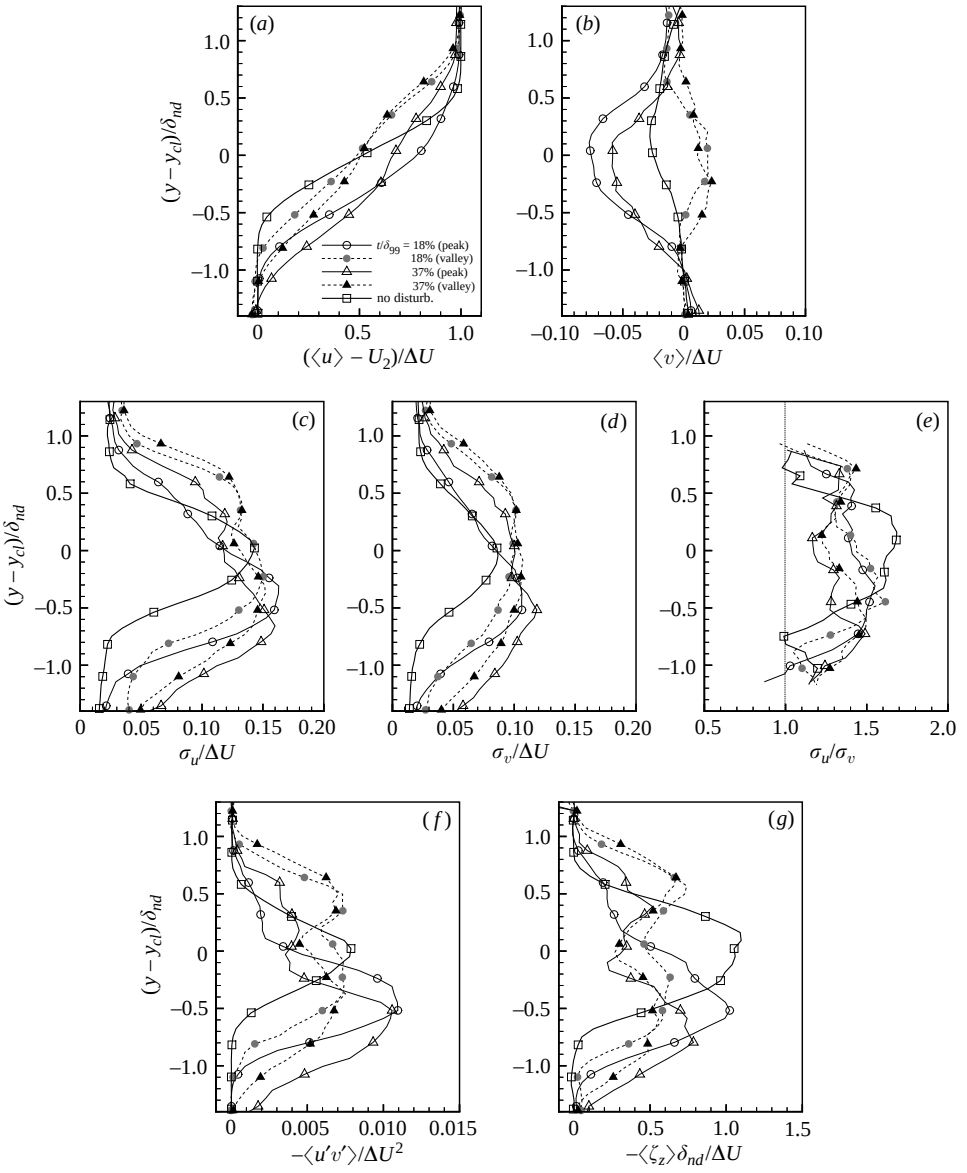

FIGURE 18. Disturbance thickness effects on transverse profiles of average velocity and turbulence statistic quantities at $M_c = 0.62$: (*a*) average streamwise velocity, (*b*) average transverse velocity, (*c*) streamwise turbulence intensity, (*d*) transverse turbulence intensity, (*e*) anisotropy, (*f*) Reynolds stress and (*g*) vorticity around the spanwise coordinate. Data for the disturbed cases ($t/\delta_{99} = 18$ and 37%) of Case 3 are shown in comparison with the no-disturbance case (Case 0).

difference in $\langle v\rangle$ between the peak and valley positions (figure 18*b*) seems to decrease slightly in accordance with the increase in the disturbance thickness. This suggests that the strength of the streamwise vortices (or the extent of induced circulation) should not be directly related to the extent of the mixing enhancement.

The disturbed cases have higher peaks of σ_u and σ_v than the no-disturbance case (figure 18*c*, *d*). Since the ratio of the increase is larger for σ_v than σ_u, the average of

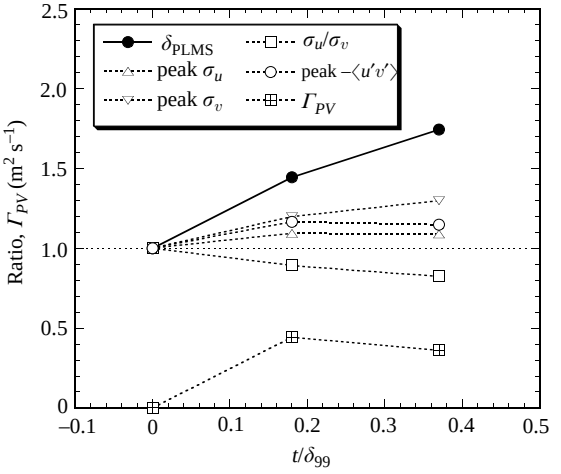

FIGURE 19. Effects of disturbance thickness (t) variation on shear-layer thickness and turbulence quantities at $M_c = 0.62$.

the turbulence anisotropy σ_u/σ_v (figure 18*e*) in the mid-shear-layer region becomes lower with increasing disturbance thickness. The increase in both σ_u and σ_v leads to a significant increase in Reynolds stress $\langle u'v'\rangle$ at the peak position (figure 18*f*), while the peak values for the two disturbed cases with different thickness are almost the same. This means that the anisotropy rather than Reynolds stress, which represents the extent of transverse transport of the streamwise momentum by turbulence, might be promising as a correlator of the effectiveness of the mixing enhancement. Observing the vorticity profile in figure 18(*g*), it is inferred that the strength of the streamwise vortex cannot be directly correlated with the effectiveness.

The effects of the disturbance thickness on the shear-layer thickness based on the PLMS results δ_{PLMS} and the other parameters at $M_c = 0.62$ are summarized in figure 19. Averages of each quantity at the peak and valley position are shown as ratios to the values for Case 0 in order to represent the overall characteristics of the shear layer considering the spanwise variation. σ_u/σ_v was calculated as an average in the mid-shear layer (half-thickness of the layer). Γ_{PV} was defined as a parameter representing the circulation induced by the streamwise vortex calculated only on the planes at the peak and valley positions, which is given by

$$\Gamma_{PV} = \left[\int_{y_U}^{y_L} \langle v\rangle \,\mathrm{d}y\right]_{peak} + \left[\int_{y_L}^{y_U} \langle v\rangle \,\mathrm{d}y\right]_{valley}. \tag{4.1}$$

As described above, the trends of the peak values of σ_u and $\langle u'v'\rangle$ and Γ_{PV} do not correlate with that of the shear-layer thickness. However, the decreasing trend of σ_u/σ_v and increasing trend of σ_v with increase in the shear-layer thickness are evident. Based on the numerical simulations of Burr & Dutton (1990), Goebel & Dutton (1991) concluded that compressibility has the effect of suppressing the pressure–transverse velocity correlation that redistributes the turbulent kinetic energy from the streamwise to the transverse direction, leading to growth-rate suppression. Vreman, Sandham & Luo (1996) also reached the same conclusion by analysing their direct numerical simulation database. Following their conclusions, it could be considered that at the moderate compressibility condition ($M_c = 0.62$), the present mixing-enhancement technique reduces the compressibility effect, which suppresses the pressure–strain-rate

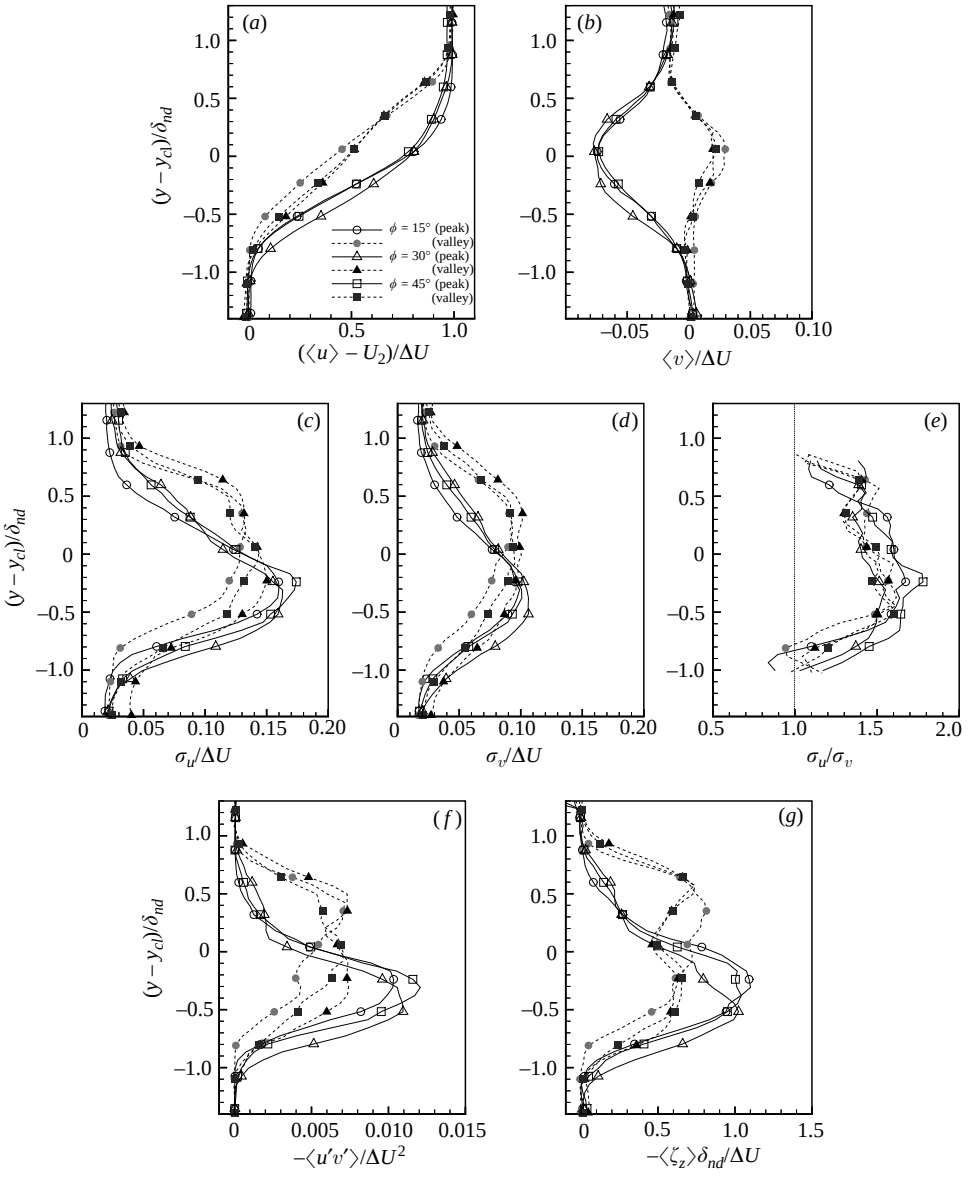

FIGURE 20. Disturbance semi-vertex angle (ϕ) effects on transverse profiles of average velocity and turbulence statistic quantities at $M_c = 0.62$: (*a*) average streamwise velocity, (*b*) average transverse velocity, (*c*) streamwise turbulence intensity, (*d*) transverse turbulence intensity, (*e*) anisotropy, (*f*) Reynolds stress and (*g*) vorticity around the spanwise coordinate. Semi-vertex angle $\phi = 15°$, 30° and 45° corresponds to Case 4, 3 and 5, respectively, with identical thickness $t/\delta_{99} = 18\%$.

redistribution, leading to the avoidance of the growth rate suppression owing to a compressibility effect.

4.2. *Effects of the semi-vertex angle of triangular disturbance*

Figure 20 presents effects of the semi-vertex angle ϕ on transverse profiles of the average velocities and turbulence quantities. Similar to the PLMS results of Island *et al.* (1998), the shear-layer thickness has a maximum value for $\phi = 30°$ (Case 3), indicating

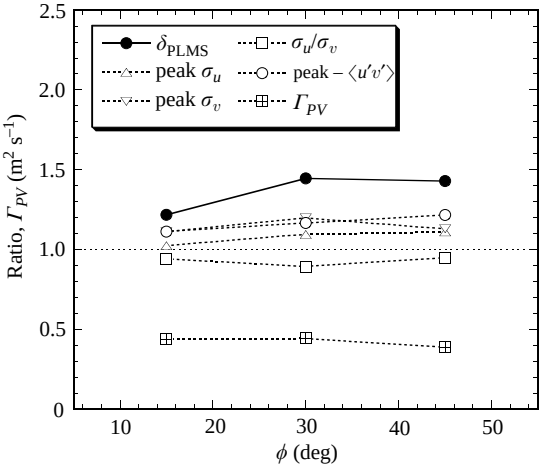

FIGURE 21. Effects of semi-vertex angle (ϕ) variation on shear-layer thickness and turbulence quantities at $M_c = 0.62$.

the optimum value of ϕ is nearly 30° at $M_c = 0.62$. For $\phi = 15°$ (Case 4), the transverse profiles of the average streamwise velocity at both peak and valley positions have only one inflection point similar to the error function profile seen for the no-disturbance case (Case 0), whereas the cases for $\phi = 30°$ and 45° (Case 5) have triple inflection points at the valley position. As shown in figure 20(*b*), the difference in the strength of the streamwise vortex is small among the three cases. Peak values of σ_u and $\langle u'v' \rangle$ at the peak position slightly increase with increase in ϕ. On the other hand, the peak value of σ_v has a maximum value for the case with $\phi = 30°$, leading to a minimum value of σ_u/σ_v in the mid-shear-layer region.

A summary of the effects of ϕ at $M_c = 0.62$ is shown in figure 21. All values in the figure are normalized by the values for the no-disturbance case. Although differences in the values are relatively small, it should be noted that the trends of σ_v and σ_u/σ_v coincide with the trend of the shear-layer thickness (having a maximum value at $\phi = 30°$) as found in the discussion on the effects of the disturbance thickness in figure 19. This finding reinforces the earlier conclusion that suppression of the increasing turbulence anisotropy with increasing compressibility might be closely related with the mechanism of the mixing enhancement.

4.3. *Effects of offset of disturbance from splitter tip*

Figure 22 compares transverse profiles of average velocities and turbulence quantities for the cases without offset (Case 3; $L_0/L = 0$) and with offset (Case 6; $L_0/L = 0.5$) as well as the no-disturbance case (Case 0). The streamwise velocity profiles for the case with offset at both peak and valley positions almost agree with the profile for the no-disturbance case. However, it can be seen from the results of $\langle v \rangle$ (figure 22*b*) that the streamwise vortex generated by the disturbance does exist for the offset disturbance while the strength is much weaker than that for the case without offset. The other turbulence quantities for the offset case are also nearly identical to those for the no-disturbance case. Therefore, we infer that the streamwise vortices generated at the leading edge of the triangular disturbances interact with the turbulent boundary layer on the splitter plate in the small area between the trailing edge of the disturbances and the splitter tip, such that the interaction greatly reduces the strength of the vortices at the splitter tip. Several disturbance configurations tested by Dolling *et al.* (1992)

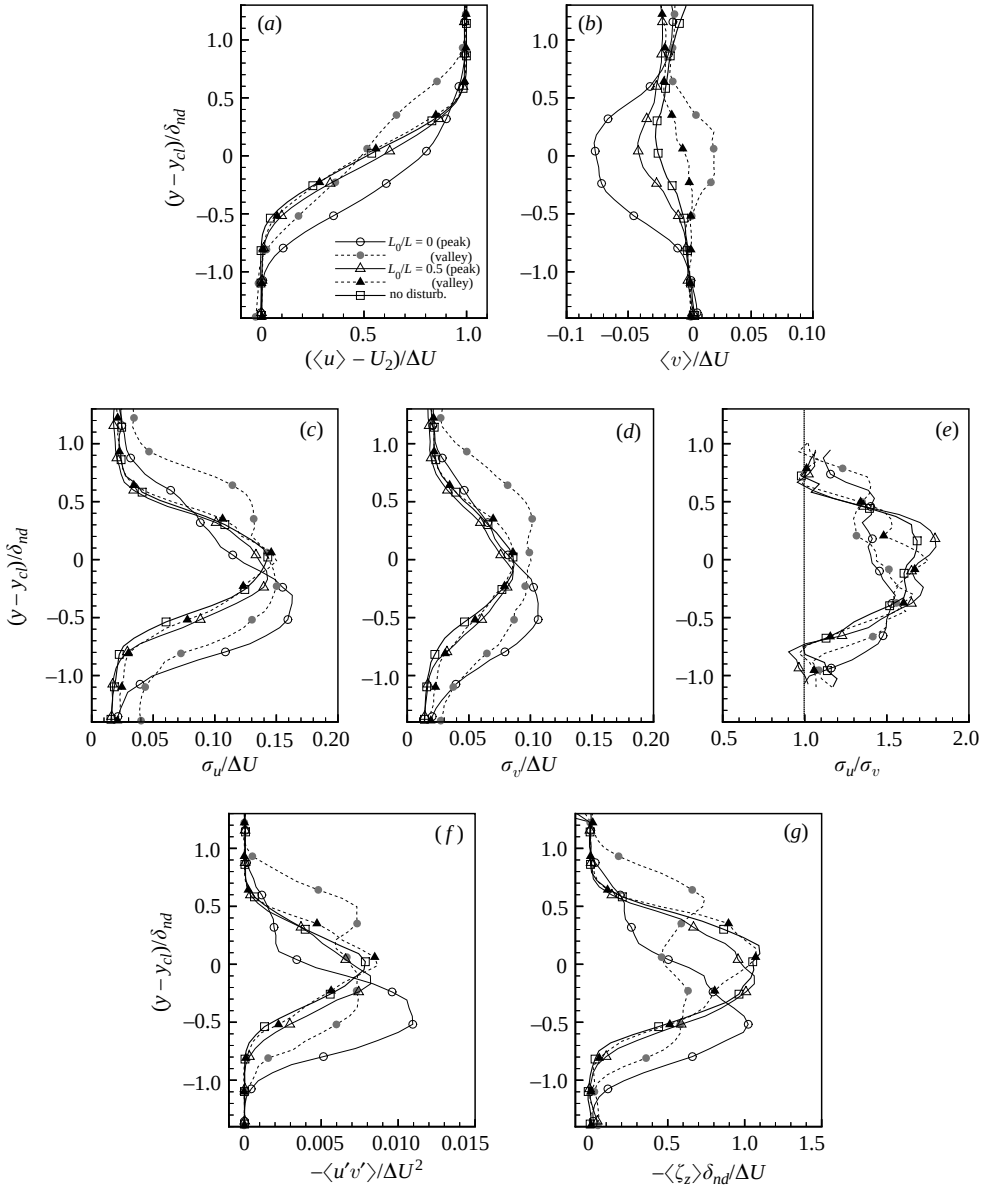

FIGURE 22. Effects of disturbance streamwise offset (L_0) on transverse profiles of average velocity and turbulence statistic quantities at $M_c = 0.62$: (*a*) average streamwise velocity, (*b*) average transverse velocity, (*c*) streamwise turbulence intensity, (*d*) transverse turbulence intensity, (*e*) anisotropy, (*f*) Reynolds stress and (*g*) vorticity around the spanwise coordinate. Streamwise offset $L_0/L = 0$ and 0.5 corresponds to Case 3 and 6, respectively, with identical equilateral planform shape and thickness $t/\delta_{99} = 18\%$.

with relatively large offsets from the splitter tip, which showed practically no growth rate increase, seem to have similar characteristics to the present results.

4.4. *Overall comparison and compressibility effects*

In figure 23, the correlation between the shear-layer thickness δ and growth rate $\mathrm{d}\delta/\mathrm{d}x$ at the imaging location x_{img} is shown for all cases tested at $M_c = 0.62$ and 0.24. Here, the thickness and growth rate were based on the PLMS panoramic side-view images by

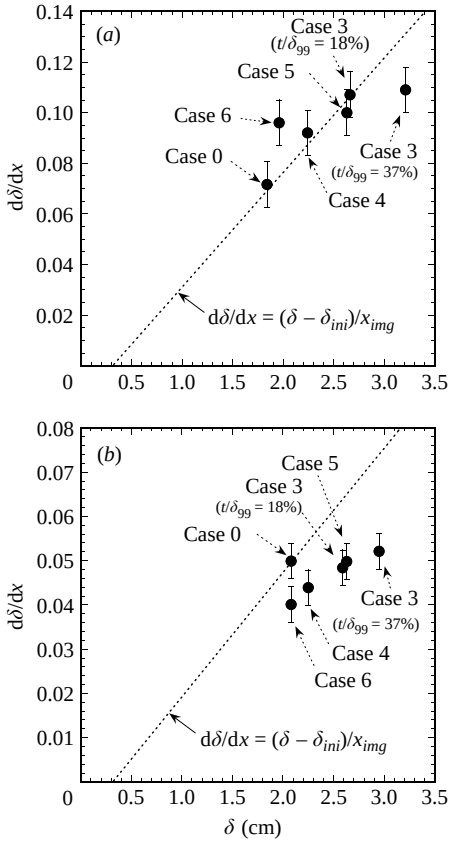

FIGURE 23. Correlation between shear-layer thickness (δ) and growth rate ($d\delta/dx$) for different disturbance configurations: (*a*) $M_c = 0.62$, (*b*) $M_c = 0.24$. δ_{ini} denotes the initial shear-layer thickness at $x = 0$. x_{img} is equal to 22 cm and 36 cm at $M_c = 0.62$ and 0.24, respectively.

averaging the values at the peak and valley positions. Straight lines in the figures show the relation between δ and $d\delta/dx$ when it is assumed that the shear layer of an initial thickness of δ_{ini} starts to develop from the splitter tip ($x = 0$) with a constant growth rate to the imaging station. Data points in the lower area of the line indicate that the growth rate decreases with downstream distance from the splitter tip to the imaging station. At $M_c = 0.62$, most data collapse close to the line, indicating the growth rate is nearly constant streamwise. On the other hand, at $M_c = 0.24$, all data points except the data for Case 0 (the no-disturbance case) fall below the line, meaning that the initial mixing-enhancement effects near the splitter tip owing to the disturbances decrease with downstream distance regardless of the disturbance configuration. Also, differences in the growth rate at the imaging location are small among the cases with various disturbance configurations, while the growth rates for Cases 4 ($\phi = 15^\circ$) and 6 ($L_0/L = 0.5$) are even smaller than the no-disturbance case. Based on these observations, it can be concluded that at the low-compressibility condition, the present strategy of mixing enhancement using the triangular disturbances with sub-boundary-layer thickness is not effective to increase the growth rate although the initial effect for thickening the shear layer just downstream of the splitter tip certainly exists. Another finding is that Case 5 ($\phi = 45^\circ$) is slightly superior to Case 3 ($\phi = 30^\circ$) at $M_c = 0.24$

while Case 3 is superior to Case 5 at $M_c = 0.62$. The result indicates that the optimum semi-vertex angle increases with decrease in the high-speed stream Mach number. The stability calculation results of supersonic boundary layers on a flat plate by Mack (1969) support this experimental result, showing that the maximum temporal amplification rate occurs for a wave propagating at 60° to the free-stream direction (which corresponds to the wave due to the disturbance of $\phi = 30°$) at $M = 2.2$, and the optimum wave angle decreases (i.e. the optimum ϕ increases) with decreasing free-stream Mach number.

Figure 24 shows the correlation between shear-layer thickness and some major parameters which are considered to be responsible for the turbulent mixing, such as turbulent quantities and the circulation induced by the streamwise vortex. The data points consist of the results for Case 0, 3 ($t/\delta_{99} = 18$ and 37%), 4, 5 and 6. Here, the shear-layer thickness measured by PLMS at the imaging station is chosen as a measure of effectiveness of the mixing enhancement since, (i) differences in the mixing efficiency due to the disturbance configuration variation are small in comparison with the shear-layer thickness difference (Island *et al.* 1998), and (ii) the growth rate measured by the PLMS results include errors which are too large to be used for this purpose. As in the former figures, the values presented in this figure are averages of the values at the peak and valley positions, and are normalized by the value for the no-disturbance case (Case 0), which is denoted by the subscript '*nd*'. Figures 24(*a*)–24(*d*) show the correlation with the peak values of turbulence intensities σ_u and σ_v, the peak value of Reynolds stress magnitude $|\langle u'v' \rangle|$, and anisotropy σ_u/σ_v averaged in the mid-shear layer. It can be observed that the turbulence intensity in terms of the transverse velocity σ_v increases and anisotropy σ_u/σ_v decreases almost linearly with increasing shear-layer thickness at $M_c = 0.62$. Again, this result also supports the conclusion that the present mixing enhancement is effectively attained through the effect of intensifying the redistribution of the turbulent kinetic energy from the streamwise to the transverse direction at the compressible condition. Although the peak values of σ_u and $|\langle u'v' \rangle|$ also show increasing trends with increase in shear-layer thickness at $M_c = 0.62$, the values stay nearly constant for large shear-layer thickness ($\delta/\delta_{nd} > 1.4$). Generally speaking, for the data at $M_c = 0.24$, a clear correlation cannot be seen for all parameters. This might suggest that the shear-layer thickness is not suitable as a measure of effectiveness of the mixing enhancement at the nearly incompressible condition, where the shear layer develops nonlinearly with streamwise distance. It should be noted that at $M_c = 0.24$ the peak value of $|\langle u'v' \rangle|$ decreases with increase in shear-layer thickness, which is opposite to the trend seen at $M_c = 0.62$.

To consider not only the peak values of the turbulence quantities, but also transverse variations of them, the turbulence intensity and Reynolds stress were integrated in the y-direction between the lower and upper boundaries, i.e. y_L and y_U, in a finite-difference manner. Using the integral values (figure 24*e*–*g*), the correlation of the shear-layer thickness with the turbulence intensities and Reynolds stress generally becomes better at both $M_c = 0.62$ and 0.24. This suggests that considering the transverse distribution of such values in the shear layer is necessary to evaluate the contribution of the parameters to the mixing enhancement. However, Reynolds stress does not correlate well with the shear-layer thickness at $M_c = 0.24$.

Figure 24(*h*) shows the correlation with the parameter representing the strength of circulation due to the streamwise vortex. Generally, as the shear-layer thickness increases, the circulation increases. Since the streamwise vortices contribute to the momentum transport across the shear layer through induced transverse fluid motions, the general trend can be understood. However, a linear correlation cannot be found.

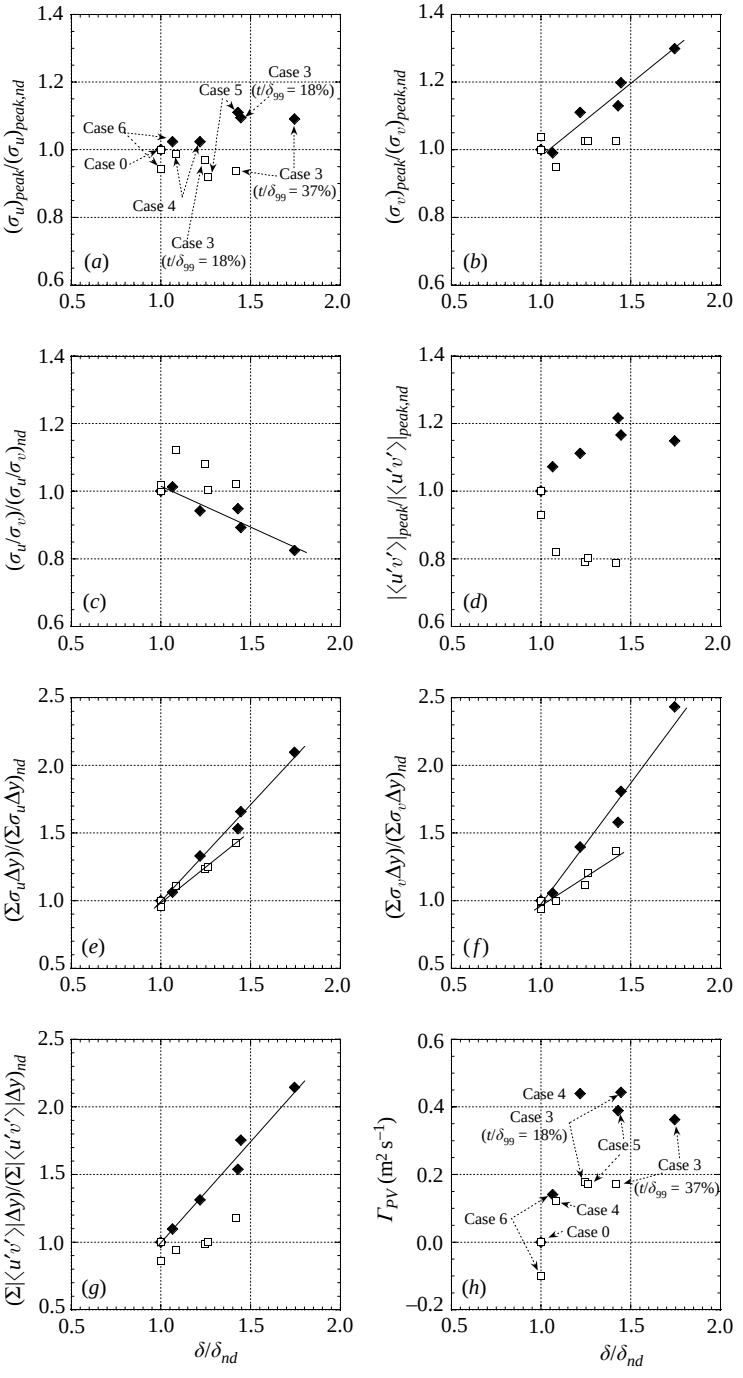

FIGURE 24. Correlation between shear layer thickness (δ) and quantities responsible for turbulent mixing for different disturbance configurations at □, $M_c = 0.24$ and ▲, 0.62: (a, b) streamwise and transverse turbulence intensity, (c) turbulence anisotropy, (d) Reynolds stress, (e, f) transverse summation of streamwise and transverse turbulence intensity, (g) transverse summation of Reynolds stress and (h) circulation parameter due to streamwise vortex (4.1). Subscripts '*peak*' and '*nd*' denote peak values in the shear layer and values for the no-disturbance case (Case 0), respectively.

Therefore, based on the present results, we cannot arrive at a clear conclusion on the relation between the strength of the induced streamwise vortex and the mixing enhancement effect. The direction of the circulation for the case with the disturbance offset (Case 6) at $M_c = 0.24$ is opposite to that at $M_c = 0.62$ and that for the case with no offset (Case 3) at $M_c = 0.24$. In this case, the vortex has an induced upward velocity at the peak position while the velocity is downward at the valley position, leading to distortion of the shear layer upward at the peak and downward at the valley. Clear understanding of this phenomenon requires further investigation on the interaction between the streamwise vortex and the boundary layer on the splitter plate.

5. Conclusions

In order to investigate the mechanism of mixing enhancement by sub-boundary-layer triangular disturbances, planar velocity fields in side- and plan-views were measured via PIV. The experiments were conducted at moderately compressible ($M_c = 0.62$) and nearly incompressible ($M_c = 0.24$) conditions to examine the effect of compressibility on the mixing enhancement. Schlieren photographs were obtained to investigate global effects of the enhancement technique on the shear-layer growth rate. PLMS was used to find the shear-layer thickness and growth rate as measures of effectiveness of the mixing enhancement. Various disturbance configurations were compared to extract key parameters responsible for the mixing enhancement. Significant findings in the present study are summarized below.

In effectively mixing-enhanced cases with the disturbances at $M_c = 0.62$, the streamwise velocity profile across the shear layer has triple inflection points. Also, as a result of the cross-sectional shape deformation of the shear layer owing to the upward and downward velocities induced by the disturbances, the streamwise velocity profile has periodic inflection points in the spanwise direction, corresponding to the spacing of the disturbances. The various inflection points appear to enhance shear-layer instability, leading to a mixing enhancement. A pair of counter-rotating streamwise vortices generated by an individual disturbance were observed for all disturbed cases at both higher and lower compressibility conditions. However, circulation induced by the streamwise vortex does not show clear correlation with the shear-layer thickness at both compressibility conditions.

At $M_c = 0.62$, the enhanced cases showed higher turbulence intensity in terms of streamwise and transverse components and Reynolds stress in the transverse (x, y)-plane, suggesting mixing enhancement effects through a larger momentum transport than the no-disturbance case. On the other hand, at $M_c = 0.24$, peak values of the turbulence quantities show little difference between the cases with and without disturbances. Another important effect of the disturbances is to suppress the turbulence anisotropy increase at $M_c = 0.62$ against the original compressibility effect of increasing the anisotropy with increasing compressibility. The turbulence anisotropy as well as the transverse turbulence intensity has almost linear correlation with the shear-layer thickness (i.e. effectiveness of the mixing enhancement) at $M_c = 0.62$, suggesting a direct contribution of the reduced anisotropy to the mixing-enhancement phenomena through reinforced pressure–strain-rate redistribution.

The present mixing enhancement technique increases shear-layer growth rate by about 50% at $M_c = 0.62$, and the rate stays almost constant in the streamwise direction. On the other hand, at $M_c = 0.24$, no distinguishable global growth rate increase was observed while shear-layer thickness becomes thicker owing to an initial mixing-enhancement effect. It is inferred that two-dimensional structures dominant in low

compressible shear layers suppress the effects of the present mixing-enhancement technique which introduces streamwise vortices, whereas highly three-dimensional structures in higher compressibility conditions are susceptible to oblique perturbations generated by the disturbances.

This work has been sponsored by the National Science Foundation whose support is gratefully acknowledged. The authors are indebted to Dr W. D. Urban for his valuable advice and support to the experiments and the data analysis, and Dr T. C. Island and Professor N. T. Clemens for their comments and useful discussion.

REFERENCES

Adrian, R. J. 1991 Particle-imaging techniques for experimental fluid mechanics. *Annu. Rev. Fluid Mech.* **23**, 261–304.

Bogdanoff, D. W. 1983 Compressibility effects in turbulent shear layers. *AIAA J.* **21**, 926–927.

Brown, G. L. & Roshko, A. 1974 On density effects and large structure in turbulent mixing layers. *J. Fluid Mech.* **64**, 775–816.

Bruun, H. H. 1995 *Hot-Wire Anemometry – Principles and Signal Analysis*. Oxford University Press.

Burr, R. F. & Dutton, J. C. 1990 Numerical modeling of compressible reacting turbulent shear layers. *AIAA Paper* 90-1463.

Chinzei, N., Masuya, G., Komuro, T., Murakami, A. & Kudou, K. 1986 Spreading of two-stream supersonic turbulent mixing layers. *Phys. Fluids* **29**, 1345–1347.

Clemens, N. T. 1991 An experimental investigation of scalar mixing in supersonic turbulent shear layers. PhD thesis, Stanford University.

Clemens, N. T. & Mungal, M. G. 1991 A planar Mie scattering technique for visualizing supersonic mixing flows. *Exps. Fluids* **11**, 175–185.

Clemens, N. T. & Mungal, M. G. 1992*a* Effects of sidewall disturbances on the supersonic mixing layer. *J. Propul. Power* **8**, 2249–2251.

Clemens, N. T. & Mungal, M. G. 1992*b* Two- and three-dimensional effects in the supersonic mixing layer. *AIAA J.* **30**, 973–981.

Clemens, N. T. & Mungal, M. G. 1995 Large-scale structure and entrainment in the supersonic mixing layer. *J. Fluid Mech.* **284**, 171–216.

Dimotakis, P. E. 1991 Turbulent free shear layer mixing and combustion. *Prog. Astronaut. Aeronaut.* **137**, 265–340.

Dolling, D. S., Fournier, E. & Shau, Y. R. 1992 Effects of vortex generators on the growth rate of a compressible shear layer. *J. Propul. Power* **8**, 1049–1056.

Dutton, J. C. 1997 Compressible turbulent free shear layers. In *AGARD Rep. 819: Turbulence in Compressible Flows*.

Elliott, G. S. & Samimy, M. 1990 Compressibility effects in free shear layers. *Phys. Fluids* A **2**, 1231–1240.

Elliott, G. S., Samimy, M. & Arnette, G. S. 1995 The characteristics and evolution of large-scale structures in compressible mixing layers. *Phys. Fluids* **7**, 864–876.

Fernando, E. M. & Menon, S. 1993 Mixing enhancement in compressible mixing layers: an experimental study. *AIAA J.* **31**, 278–285.

Ferri, A. 1973 Mixing-controlled supersonic combustion. *Annu. Rev. Fluid Mech.* **5**, 301–338.

Foss, J. K. & Zaman, K. B. M. Q. 1999 Large- and small-scale vortical motions in a shear layer perturbed by tabs. *J. Fluid Mech.* **382**, 307–329.

Freund, J. B., Lele, S. K. & Moin, P. 2000 Compressibility effects in a turbulent annular mixing layer. Part 1. Turbulence and growth rate. *J. Fluid Mech.* **421**, 229–267.

Goebel, S. G. & Dutton, J. C. 1991 Experimental study of compressible turbulent mixing layers. *AIAA J.* **29**, 538–546.

Gruber, M. R., Messersmith, N. L. & Dutton, J. C. 1993 Three-dimensional velocity field in a compressible mixing layer. *AIAA J.* **31**, 2061–2067.

Gutmark, E. J., Schadow, K. C. & Yu, K. H. 1995 Mixing enhancement in supersonic free shear flows. *Annu. Rev. Fluid Mech.* **27**, 375–417.

Island, T. C. 1997 Quantitative scalar measurements and mixing enhancement in compressible shear layers. PhD thesis, Stanford University.

Island, T. C., Urban, W. D. & Mungal, M. G. 1998 Mixing enhancement in compressible shear layers via sub-boundary layer disturbances. *Phys. Fluids* **10**, 1008–1020.

Karasso, P. S. & Mungal, M. G. 1996 Scalar mixing and reaction in plane liquid shear layers. *J. Fluid Mech.* **323**, 23–63.

Lele, S. K. 1994 Compressibility effects on turbulence. *Annu. Rev. Fluid Mech.* **26**, 211–254.

Mack, L. M. 1969 Boundary layer stability theory. *Jet Propulsion Lab. Preprint* 900, 277.

Menon, S. 1989 Shock-wave induced mixing enhancement in scramjet combustors. *AIAA Paper* 89-0104.

Miller, M. F. 1994 An experimental investigation of the effect of compressibility on a turbulent reacting mixing layer. PhD thesis, Stanford University.

Nygaard, K. J. & Glezer, A. 1991 Evolution of streamwise vortices and generation of small-scale motion in a plane mixing layer. *J. Fluid Mech.* **231**, 257–301.

Olsen, M. G. & Dutton, J. C. 2003 Planar velocity measurements in a weakly compressible mixing layer. *J. Fluid Mech.* **486**, 51–77.

Papamoschou, D. & Roshko, A. 1988 The compressible turbulent shear layer: an experimental study. *J. Fluid Mech.* **197**, 453–477.

Prasad, A. K., Adrian, R. J., Landreth, C. C. & Offutt, P. W. 1988 Measurement and refinement of velocity data using high image density analysis in particle image velocimetry. In *Proc. Fourth Intl. Symp. Applications of Laser Anemometry to Fluid Mechanics, Lisbon, Portugal*, pp. 485–497.

Ragab, S. A. & Wu, J. L. 1989 Linear instabilities in two-dimensional compressible mixing layers. *Phys. Fluids* A **1**, 957–966.

Samimy, M., Erwin, D. E. & Elliott, G. S. 1989 Compressibility and shock wave interaction effects on free shear layers. *AIAA Paper* 89-2460.

Samimy, M. & Lele, S. K. 1991 Motion of particles with inertia in a compressible free shear layer. *Phys. Fluids* A **3**, 1915–1923.

Sandham, N. D. & Reynolds, W. C. 1990 Compressible mixing layer: linear theory and direct simulation. *AIAA J.* **28**, 618–624.

Sandham, N. D. & Reynolds, W. C. 1991 Three-dimensional simulations of large eddies in the compressible mixing layer. *J. Fluid Mech.* **224**, 133–158.

Sato, N., Imamura, R., Shiba, S., Takahashi, M., Tsue, M. & Kono, M. 1999 Advanced mixing control in supersonic airstream with a wall-mounted cavity. *J. Propul. Power* **15**, 358–360.

Swithenbank, J., Eames, I. W., Chin, S. B., Ewan, B. C. R., Yang, Z., Cao, J. & Zhao, X. 1991 Turbulent mixing in supersonic combustion systems. *Prog. Astronaut. Aeronaut.* **137**, 341–381.

Urban, W. D. 1999 Planar velocity measurements in compressible mixing layers. PhD thesis, Stanford University.

Urban, W. D. & Mungal, M. G. 1997 Planar velocity measurements in compressible mixing layers. *AIAA Paper* 97-0757, 35th Aerospace Sciences Meeting, Reno, NV.

Urban, W. D. & Mungal, M. G. 2001 Planar velocity measurements in compressible mixing layers. *J. Fluid Mech.* **431**, 189–222.

Urban, W. D., Watanabe, S. & Mungal, M. G. 1998 Velocity field of the planar shear layer: compressibility effects. *AIAA Paper* 98-0697, 36th Aerospace Sciences Meeting, Reno, NV.

Vreman, A. W., Sandham, N. D. & Luo, K. H. 1996 Compressible mixing layer growth rate and turbulence characteristics. *J. Fluid Mech.* **320**, 235–258.

Watanabe, S. & Mungal, M. G. 2000 An experimental investigation on mixing-enhanced compressible shear layers. ISTS paper 2000-e-12, *22nd Intl Symp. on Space Technology and Science, Morioka, Japan.*